# Chapter 3
# Multiscale Modelling of Mechanical Anisotropy

**Jerzy Gawad, Albert van Bael and Paul van Houtte**

## 3.1 Introduction

Let us first recall one of the most fundamental observations in the material science and engineering: the overall chemical composition of a material does not fully determine the properties of the material. The internal structure of the material, which can be observed on the microscopic scale, influences its macroscopic properties as well. The term 'microstructure' is commonly used when referring to that structure, yet the meaning of the term remains somewhat ambiguous. In the first place, the definitions of the microstructure vary from one research field to another. The differences in what is understood by the term reach down to the list of features that are considered as belonging to the microstructure. Even the length scale associated with the microstructure is not unambiguously defined, although the name itself suggests that order of micrometers would be the proper scale.

The original version of the chapter was revised: The erratum to this chapter is available at 10.1007/978-3-319-44070-5_8

J. Gawad (✉)
Department of Computer Science, KU Leuven,
200A Celestijnenlaan, 3001 Leuven, Belgium
e-mail: jerzy.gawad@cs.kuleuven.be
URL: http://www.kuleuven.be/english

A. van Bael · P. van Houtte
Department of Materials Engineering, KU Leuven,
44 Kasteelpark Arenberg, 3001 Leuven, Belgium
e-mail: albert.vanbael@mtm.kuleuven.be
URL: http://www.kuleuven.be/english

P. van Houtte
e-mail: paul.vanhoutte@mtm.kuleuven.be



D. Banabic (ed.), *Multiscale Modelling in Sheet Metal Forming*,
ESAFORM Bookseries on Material Forming,
DOI 10.1007/978-3-319-44070-5_3

This chapter does not attempt to define the microstructure as such. We will rather follow the notion of microstructure-property relationships. From this point of view, the microstructure includes all features of the material needed to explain a certain property of interest. By the same token, the microstructure contains all information needed to *derive* or *compute* that property. This notion of deriving properties by means of microstructure simulations is nowadays well accepted, see for example the textbook by Ghosh and Dimiduk (2011).

The mechanical behaviour of polycrystalline metals and alloys is controlled by several factors generally attributed to the microstructure of the material. To enumerate just a few most recognized in the literature:

- phase composition,
- crystal structure of the phases, which also determines the deformation mechanisms of each phase,
- grain size and shape,
- preferential orientation of the crystals, usually referred to as crystallographic texture,
- substructure, which is typically a self-organized dislocations pattern,
- interfaces of the phases and grain boundaries,
- presence of non-metalic or intermetalic phases,
- presence of voids and other imperfections at the grain boundaries,
- presence of micro-cracks and other intra-grain discontinuities.

This short enumeration can already give us an impression what order of complexity one has to deal with to derive the properties from the microstructure. Most of these factors cannot be considered in isolation, which makes the matters yet more convoluted. Another source of difficulty intrinsically lies in hierarchical nature of polycrystalline materials: larger structures have a substructure (Fig. 3.1). A length scale suitable to tackle phenomena occurring in the structure is rarely convenient to concurrently analyse the substructure. Even if we limit our interest to plasticity, it remains a highly coupled phenomenon which involves at least large part of the factors listed above. Certain factors have a direct consequence on the plastic

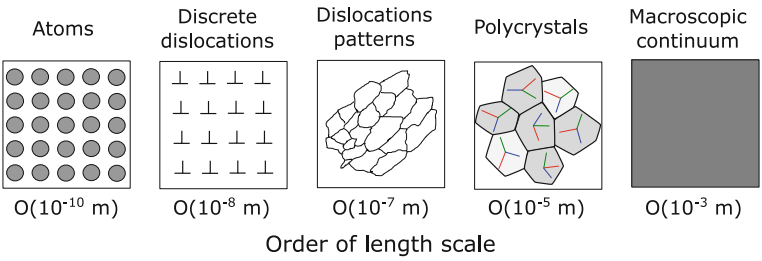


**Fig. 3.1** Hierarchy of length scales in metallic materials: from macroscopic, via multiple differently oriented crystals, via patterns of dislocations (substructure), via dislocation cores, to atomistic level. Different modelling and simulation methods are used at each length scale

deformability of the material. For instance, the crystal lattice largely determines the available deformation mechanisms. Some types of crystals may primarily deform by crystallographic slip, other tend to accommodate the deformation also by activating twinning mechanisms. It is also possible that a crystal subjected to an external mechanical loading may also undergo a phase transformation. Yet the crystal structure alone does not give us a complete picture. The activation of the crystallographic deformation mechanisms largely depends on the direction of loading, which means the crystals are mechanically anisotropic. As we can see, there is a link between microstructure and micro-scale properties. If an aggregate comprising a finite number of individual crystals is deformed, its mechanical anisotropy depends on the orientation of the constituents. Therefore, the crystallographic texture, which is a microstructural feature, influences the mechanical anisotropy of polycrystalline. This brings us to the clue that a link between the microstructure and effective properties observed in a lager scale can be also derived. In other words, a microstructure can be exploited to characterize a homogeneous continuous medium (Miehe et al. 1999). Note that the effective properties are usually associated with a constitutive description of the material in continuum mechanics, and as such are very much applicable in numerous engineering problems, including simulation of metal forming.

It is extremely complex to directly include some of microstructural features in continuum mechanics constitutive modelling. For instance, reorientation of individual crystals due to deformation is hard to describe in that manner. Thus, another theoretical framework is needed to derive homogenized properties from the microstructure. It is useful to introduce two different phenomenological scales:

- *micro-scale* that is characterized by a statistically representative volume of material that comprises microstructural constituents. An assembly of microstructural features enumerated above can be conveniently modelled in this scale.
- *macro-scale* that considers the material as a continuous medium.

The two scales can be more generally named as *fine-scale* and *coarse-scale*, respectively, but the terms micro-scale and macro-scale put more emphasis on the relation with the microstructure. For this reason we will only occasionally use the generic names in this chapter. A two-level hierarchy, nevertheless, constitutes one of fundamental building blocks of a more general multi-scale approach.

It is important to note that state variables used in the micro- and macro-scale are typically different, but some of the variables have counterparts in both scales, as presented in Fig. 3.2. This framework is commonly known as Representative Volume Element (RVE), sometimes also referred to as Representative Elementary Volume. The RVE concept is one of the foundations of homogenization theories.

In essence, the RVE is considered as a sub-volume of the whole bulk of material. The RVE allows one to estimate statistically representative coarse-scale responses

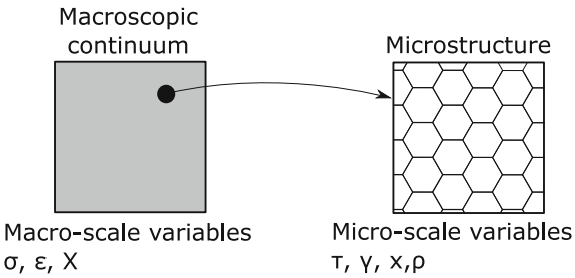


**Fig. 3.2** Continuum with micro-structure modelled as RVE. A typical point in the macro-scale is characterized by a representative assembly of microstructural elements. The relations between variables in the coupled scales may vary. For instance, state variables $\sigma, \epsilon$ in the macroscale are defines as volume averages of $\tau, \gamma$ in the micro-scale, respectively, the variable $X$ is a direct counterpart of micro-scale variable $x$, whereas the variable $\rho$ is relevant only in the micro-scale

or properties of a heterogeneous volume where fine-scale evolution laws hold. A prerequisite needed for this coupling is that a sufficient scale separation must be satisfied (Ostoja-Starzewski 2005, 2006). In other words, an RVE has to be large enough compared to the characteristic length scale of its constituents and processes altering the constituents. Since the RVE is supposed to generate a description that represents the whole material, it must include a sufficient sampling of the variety of microstructural features that exist in the material. This implies that the minimal size of an RVE must be set in such a way that any smaller sub-volume would be insufficient to statistically represent the variation of its constituents. An RVE needs also to satisfy the requirement that further increase of its size does not significantly change the resulting homogenized response or properties (McDowell 2010). As a corollary, a properly constructed RVE shall approximately provide the same response and properties as any other proper RVE.

A natural question arises what is the proper size of the RVE if random polycrystals are modelled. A closely related question is how many grains are necessary to homogenize the response of polycrystalline aggregates. It is essential to realize that the necessary size of an RVE depends on the type of responses and effective properties accounted for. These may present considerably different sensitivity to the microstructural composition of the RVE. The factors that play a role in this context typically include spatial distribution of microstructural constituents inside the RVE, grain size distribution, as well as phase contrast with respect to certain properties. Furthermore, the required RVE size is also influenced. For instance, the elastic properties (the elastic moduli) or responses (such as stiffness) in non-evolving stationary microstructures are less sensitive to local configurations of the constituents than plastic properties in evolving microstructures (McDowell 2010). Therefore, for the same microstructure, the RVE size differs depending on what effective properties are considered (Kanit et al. 2003).

## 3.2 Multiscale Frameworks in Crystal Plasticity

As we have discussed in the previous section, the plastic anisotropy, as well as many other properties of polycrystalline metals, is controlled by the microstructure. Several microstructural factors are involved, yet crystallographic texture is often the most prevailing feature in this respect. Given its importance, the literature contains a broad variety of reported attempts to take the texture into account in numerical simulations of metal forming processes. Broadly speaking, the microstructure can be explicitly dealt with if a physics-based model is employed to resolve deformation mechanisms in individual crystals. This can be done along with homogenizing the response over a polycrystal. Several crystal plasticity (CP) frameworks exist that allow one not only to derive macroscopic mechanical response of polycrystalline materials, but that also provide insights on how the microscopic state evolves with an increasing deformation. The crystal plasticity frameworks are typically used in one of the following contexts:

- We can use a crystal plasticity framework at the micro-scale, where the microstructure of a small volume of material is represented in a much detailed manner. If the microstructure is explicitly modelled and discretized (either in 2D or 3D), the resolution of the discretization is sufficiently fine to study intra- and inter-granular effects. The RVE method is typically used in this case to obtain effective properties or responses of the microstructure.
- We can also directly use a crystal plasticity framework inside a macroscopic simulation. Although various microstructural features (such as texture evolution, plastic slip, phase transformation etc.) can be tracked, the spatial resolution is usually coarser than in the previous case and typically enables tackling whole grains. Properties of the material or the constitutive relations needed by the macroscopic simulation are directly extracted from the crystal plasticity framework. The direct coupling may follow the RVE approach, but direct embedding is also possible.
- We can combine the two ways and indirectly employ a crystal plasticity framework inside a macroscopic simulation. The microstructure evolution is dealt with by a crystal plasticity RVE, while some other means are used to get the properties or responses needed in the calculations of the macroscopic model. For instance, an approximation function can be fitted to the responses of interest calculated by the RVE. The approximation can be either calculated before the macroscopic simulation starts (i.e. as a part of pre-processing), or during the simulation. The latter case can also include adjusting the approximation to the evolved microstructural state as the macroscopic simulation advances.

The two first approaches are somewhat complementary, but their focus is different. Whereas the former usually attempts to elucidate *why and how* certain fine-scale interactions develop and *how* they impact the coarse-scale, the latter usually tries to answer only the second question. Conversely, the third approach is based on a different paradigm: given a sufficiently predictive CP framework, a computationally efficient coupling has to be established to answer both questions at once.

Several crystal plasticity frameworks have been proposed over the last decades to answer these challenges. In this chapter we shall restrict the discussion to those that explicitly deal with microstructure to recover the properties of interest. We will put particular emphasis on several existing strategies to incorporate the texture data into macroscopic Finite Element simulations.

At this point we only remind the reader that another approach to handle plastic anisotropy exists: phenomenological models that neglect the microstructural evolution and restrict their scope to the macroscopic mechanical response of the material. Chapter 1 provides an extensive overview of models belonging to this category.

## *3.2.1 Statistical Crystal Plasticity*

The RVE concept can be used even if the microstructure is not fully resolved in 3D, but in a statistical manner as a set of crystals. This approach is often called statistical or mean-field crystal plasticity.

### 3.2.1.1 Sachs-Type Models

The iso-stress model (also called "static model"), which is commonly attributed to Sachs (1928),[1] assumes that the stress mode is the same in all crystals of a polycrystalline aggregate. It is then possible to apply the Generalized Schmid law (see Chap. 2 and Gottstein (2004) for comprehensive explanation of the Schmid law) to each of the crystals. It would then be found, at gradually increasing stress level, that at first there would be no plastic deformation anywhere, until a stress level is reached for which plastic deformation would start in the grain or grains with the most favorable lattice orientation. Since all the grains experience the same state of stress, the plastic deformation that results from it can vary from one grain to another, thus the compatibility conditions in the aggregate are violated. The iso-stress assumption is nowadays considered as an oversimplification, so this group of models is rarely used.

[1] In fact, the work by Sachs (1928) does not assume a uniform stress field in the polycrystal, but it considers a uniaxial tensile test on a polycrystalline material, where the Schmid law (for a uniaxial tensile test!) is applied to find the first activated slip system in all grains, treated as stand-alone single crystals in which one slip system is activated. Sachs proposed a model that assumes the average of all local flow stresses to be the macroscopic flow stress (also tensile, of course).

#### 3.2.1.2 Taylor-Type Models

The Full Constraints (FC) Taylor-Bishop-Hill homogenization scheme, which was originally proposed by Taylor (1938) and later taken up again by Bishop and Hill (1951a), who proposed a different but equivalent solution method, assumes identical plastic deformation throughout all the grains in the considered volume of the material. The constitutive equations are thus formulated for a single grain that is considered in isolation. Although the compatibility conditions are automatically satisfied since the entire aggregate experiences the same state of deformation, yet the stress equilibrium condition is neglected. These authors proposed two different solution methods, which are both based on the Generalized Schmid Law as the constitutive model for a metallic crystal. An approximate but mathematically convenient alternative is the visco-plastic method by Asaro and Needleman (1985).

It is well recognized that the Full Constraints approach overestimates both texture intensity and the homogenized stresses. To answer these limitations, several improvements have been proposed, among which the Relaxed Constraint Taylor (RCT) (Raphanel and Van Houtte 1985; Van Houtte 1982, 1987, 1988). The relaxed constraints models drop Taylor's strict requirement of strain homogeneity and allow certain violations in compatibility conditions. In other words, relaxations are imposed on certain components of the velocity gradient tensor. Although the RCT scheme led to moderate improvements in predictability, the concept itself turned out to be quite influential.

#### 3.2.1.3 Grain Interaction Models

The relaxations are the core part of so-called 'cluster' models (also known as 'grain interaction models'), which define more elaborated homogenization schemes. The homogenization deals with small clusters of grains in place of single crystals. It is assumed that the average plastic velocity gradient of the cluster is equal to the macroscopic velocity gradient. Therefore, the 'cluster' models abandon the assumption that each grain is treated separately and introduce interactions between crystals in the aggregate.

The Advanced LAMEL (ALAMEL) model was proposed by Van Houtte et al. (2005) as a generalization of the LAMEL (Liu et al. 2002; Van Houtte et al. 1999). The ALAMEL model considers interactions in clusters of two grains, separated by an interface, which represents a grain boundary. The interface can be arbitrarily oriented according to a certain distribution function. In the ALAMEL scheme local strains deviate from the macroscopic strain according to admissible relaxation modes, and the extent of the relaxation is calculated by minimizing the collective plastic work inside the cluster. Several improvements to the ALAMEL model scheme have been recently proposed, for example by Arul Kumar et al. (2011), Mahesh (2010), Mánik and Holmedal (2013), Zhang et al. (2014). The multisite approach (Delannay 2002; Delannay et al. 2002, 2009; Van Houtte et al. 2002), which extends the ALAMEL, postulates that each grain interacts exclusively with

one or several of the surrounding grains. Furthermore, it adds elastic part to the governing equations.

A similar model was proposed by Evers et al. (2002), who used the RTC homogenization to calculate deformation of bi-crystal volume elements, each having the crystallographic lattice orientations of two adjacent crystals.

The Grain InterAction (GIA) model, which also puts forward the concept of grain clusters, was proposed by Crumbach et al. (2001) and further elaborated by Engler et al. (2005). The GIA model takes into account short-range interactions between next-neighbour grains in an aggregate consisting of eight hexahedral grains. The structure of GIA was further developed as the Relaxed Grain Cluster (RGC) model by Eisenlohr et al. (2009a, b), Tjahjanto et al. (2010, 2015). It was recently extended to deal with multi-phase materials (Tjahjanto et al. 2015).

#### 3.2.1.4 Self-consistent Schemes

The Visco-Plastic Self-Consistent (VPSC) (Lebensohn and Tomé 1993; Lebensohn et al. 2007; Molinari et al. 1987, 1997) model was originally inspired by Eshelby's (1957) analytical solution of elasticity problem for an ellipsoidal inclusion embedded in an effective medium. In the VPSC the effective medium comprises all the grains in the representative volume and it is considered homogeneous. The individual crystals are treated as plastically deformable ellipsoidal inclusions constrained by the medium, so short-range interactions are basically neglected. However, the model resolves long-range interactions the in the polycrystalline, which originate in the contributions from all the crystals and are carried by the medium. The VPSC model imposes both strain compatibility and stress continuity between grains and their surrounding, as opposed to the Taylor-type models that postulate homogeneous strain in the sample (possibly with relaxations). The VPSC model has gained numerous applications, most remarkably to successfully simulate the deformation of hcp materials, e.g. Beausir et al. (2008), Ebeling et al. (2009), Plunkett et al. (2006), Steglich et al. (2012), Tomé (2001), Walde and Riedel (2007a), Wang et al. (2010) and extensions, see e.g. Knezevic et al. (2013a).

### *3.2.2 Full-Field Approaches*

Here, "full-field" denotes a category of models that make use of a discrete grid to compute certain fields variables (e.g. stress or strain) in the microstructure. The models that belong to this category resolve both long-range and short range interactions. In particular, if a sub-grain resolution of the grid is used, heterogeneities of these fields inside individual crystals can also be considered. Therefore, the full-field approaches apply crystal plasticity theories to predict the actual micromechanical fields that develop inside the grains of a polycrystal.

Consequently, various localized phenomena, such as orientation gradients inside individual grains, can be calculated as well.

The models belonging to this group are usually much more computationally demanding than the statistical models presented in the previous section, although the increase in computing performance over the last decade has allowed conducting statistically meaningful simulations.

As a general remark, the ability to include intra-granular state variables, in particular strain and stress fields, is supposed to enhance the accuracy of microstructure evolution predictions. However, as it was shown in recent studies (see e.g. Héripré et al. 2007; Pokharel et al. 2014; St-Pierre et al. 2008), comparison with intra-granular strain measurements often shows only qualitative agreement suffering clear local discrepancies between modelling and experimental results (Pinna et al. 2015). This can be attributed to various factors, including simplifications in reproducing the initial microstructure, since simulations of more controllable oligocrystals typically deliver better agreement with experiments (Delaire et al. 2000; Klusemann et al. 2012, 2013; Lim et al. 2011, 2014; Raabe et al. 2001; Turner et al. 2013; Zhang et al. 2015a). It has also been shown that the full field models do not necessarily provide considerably better predictions than the statistical ones, neither with respect to texture evolution (see e.g. Li et al. 2004) nor macroscopic anisotropy (see e.g. Zhang et al. 2015b).

#### 3.2.2.1 Crystal Plasticity Finite Element Method

A large body of work exists on incorporating crystal plasticity frameworks as constitutive relation in the Finite Element method. An excellent review of these attempts has been published by Roters et al. (2010a, b). The reader is referred to these works for a comprehensive overview of the constitutive laws, kinematics, homogenization and multiscale methods in the CP-FEM modeling.

Generally, CP-FEM resolves the equilibrium of the forces and the compatibility of the displacements based on a weak form of the principle of virtual work. This is in essence what the Finite Element method does. What differentiates the CP-FEM is the incorporation of a certain crystal plasticity constitutive law to provide the constitutive behavior of the material. This law typically include calculating the slip and twinning activity and the resulting material flow. Constitutive models extending the works of Asaro (1983a, b), Asaro and Rice (1977), Peirce et al. (1982, 1983) are very commonly used and include visco-plastic, elasto-viscoplastic and elastic-plastic constitutive behaviour. Plastic deformation of the material and evolution of texture results from activation of deformation mechanisms, such as slip and twinning. The CP-FEM models are formulated as either rate-dependent or rate-insensitive with respect to the material response. The hardening at the level of crystallographic slip and twinning is taken into account as well. A power law is often chosen to relate the applied resolved shear stress on the slip or twinning system to the shear rate in the slip or twinning direction. Large inelastic deformation can be reached in CP-FEM. However, we have to keep in mind that

accuracy of the FE method may be undermined if large distortions of elements are experienced. This issue can be addressed by advanced mesh refinement methods, see e.g. Quey et al. (2011), Resk et al. (2009).

In CP-FEM the FE mesh represents an aggregate of grains, each having a specific set of attributes, such as shape, orientation, phase, etc. The method offers several advantages over statistical approaches. Most remarkably:

- If several finite elements constitute a grain, the gradients of stress and strain inside individual crystal can be taken into account. This holds even if low order elements (e.g. linear) are used to discretize the domain.
- Gradients of other fields inside the grains can be captured as well. For instance, crystal orientation gradient may be accounted for, which is crucial in modelling intra-granular localization processes.
- Complicated geometry of individual crystals can be explicitly dealt with in the model.
- Since the grains are spatially bound by each other, explicit grain boundaries are introduced in the model. This also allows to take into consideration grain boundary properties.
- Boundary conditions can be imposed on the RVE in a flexible manner.

Despite of all these advantages, the CP-FEM is rarely considered as a feasible approach in modelling component-scale sheet forming processes. Since the number of elements in the RVE grows with the number of grains considered, simulation of the deformation becomes extremely computationally expensive for the solution of complex problems at the macroscopic level. For example, let us consider a realistic size of a cubic three dimensional RVE being 500 nodes at each edge, which transforms into $N = 500^3$ elements. For the sake of simplicity, suppose that the number of DOF required in an FEM calculation is roughly of the same order as the total number of elements. To solve the displacement field at each given deformation increment, one has to invert a matrix of the size of order $N^2$. This gives us sufficient estimate of the huge computational cost of the CP-FEM.

#### 3.2.2.2 Crystal Plasticity FFT

Recently, considerable attention has been attracted by the Crystal Plasticity Fast Fourier Transform (CP-FFT) method (Eisenlohr et al. 2013; Lebensohn 2001; Lebensohn et al. 2004, 2011, 2012; Liu et al. 2010; Prakash and Lebensohn 2009; Roters et al. 2012; Shanthraj et al. 2015), which promises substantial improvement over the CP-FEM in terms of calculation time, while keeping high spatial resolution in order to capture the details of complex microstructures. As opposed to the CP-FEM, the CP-FFT is meshless, so it uses voxels to discretize 3D domain.

The CP-FFT-based formulation consists in finding a strain-rate field, associated with a kinematically admissible velocity field, that minimizes the average of local work-rate, under the compatibility and equilibrium constraints (Lebensohn et al.

2008). The method is based on the fact that the local mechanical response of a heterogeneous medium can be calculated as a convolution integral between Green functions associated with appropriate fields of a linear reference homogeneous medium and the actual heterogeneity field. This approach is suitable for finding the solution of a unit cell problem with periodic boundary conditions. If a periodic medium is considered, one can use the Fourier transform to reduce convolution integrals in real space to simple products in Fourier space. Thus, the Fast Fourier Transform algorithm can be utilized to transform the heterogeneity field into Fourier space. Afterwards, the mechanical fields can be calculated by applying the transformation back to real space.

The CP-FFT has several advantages over the CP-FEM. It basically eliminates the major computational bottlenecks of the CP-FEM, namely the need for inverting large matrices. In addition, no advanced meshing is needed to discretize the domain since the method is meshless and requires just a simple regular grid of voxels. This also eliminates several related issues, such as degeneration of finite elements on excessive localized deformation. On the disadvantage side, the grid in Fourier space is assumed to be regular, which is less flexible in discretizing complex geometries than a free FE mesh. To date, the CP-FFT solvers can only make use of uniform grid, which might be too coarse to properly approximate stress and strain fields near grain boundaries. To keep the grid regular, simplifications to the kinematic equations have to be made (Liu et al. 2010; Prakash and Lebensohn 2009). Moreover, the fundamental requirement of periodic boundary conditions renders the CP-FFT somewhat less flexible than the CP-FEM. The CP-FEM also permits local mesh refinements to capture localization of strain and abrupt discontinuities of material properties.

## 3.3 Multi-scale Modelling of Plastic Anisotropy

All crystal plasticity frameworks presented in the previous section are inherently multi-scale: they are designed to predict coarse-scale effects of fine-scale interactions in the microstructure upon imposed coarse-scale boundary conditions. Nonetheless, the macroscopic boundary conditions that are inflicted on a simulated microstructure are relatively simple, either with respect to the geometry (e.g. displacements imposed on a face of a unit cube), or with regard to fundamental assumptions on geometry (e.g. periodicity of the system, thus a unit cube with periodic boundary conditions is assumed), or other basic assumptions in the model (e.g. identical strain everywhere in the material). Even if completely arbitrary boundary conditions can be prescribed, it is not always obvious how to choose the ones that would be most relevant in a given sheet forming process. Typical idealizations, such as plane strain deformation, pure shear, uniaxial tension/compression etc. are often just very rough approximations of the actual conditions, which are nearly always affected by the geometry of the process (including for instance shape of the sheet and the dies) as well as contact conditions and other sources of non-linearities.

For this reason it is usually not straightforward to use any of these models in simulations of sheet forming processes. The CP model can be still used as a component of a macroscopic analysis if it is provided with realistic boundary conditions. To this end, a proper coupling or embedding scheme must be established. In particular, the Finite Element Method, which is nowadays an indispensable engineering tool, has been successfully used as a macroscopic host framework for various CP models. In this section we shall present an overview of the most prominent coupling techniques.

### *3.3.1 Direct Micro-Macro Coupling*

If a micro-scale full field model is available as an RVE, one may use it as a constitutive model in a macroscopic FE simulation. In fact, direct coupling typically discards the notion of deriving properties from RVE, since the micro-model replaces the entire constitutive law, and not just the parameters in a constitutive equation. Thus, it is the homogenized RVE *response* that becomes then an integral part of the macroscopic model.

#### 3.3.1.1 Embedded Full-Field Models

Provided that an FEM RVE is coupled with a macroscopic FE model, this computational framework is called multi-level FEM (ML-FEM) (Smit et al. 1998) or $FE^2$ (Feyel 1999, 2000; Feyel and Chaboche 2003). Within this general framework one conducts an embedded micro-scale RVE FE computation in order to extract from the RVE the quantities required at integration points of the macroscale finite element mesh.

In the simplest variant, the coupling is rather straightforward. The multi-level FE computes the displacement fields on both macroscopic and microscopic level (Smit et al. 1998). The micro-scale FE RVE provides the homogenized stiffness matrix, which is returned to the corresponding integration point in the macroscopic mesh as the local macroscopic tangential stiffness matrix.

Such embedding scheme has a clear advantage: no analytical constitutive equation needs to be specified at the macroscopic scale, since the constitutive behaviour comes directly from the microscale. For certain types of materials, such as multi-phase steels, constitutive equations that account for the presence of multiple phases are very difficult to specify. The use of ML-FEM bypasses this problem because all the complexity of a multi-phase material is handled by the micro-scale FE simulation.

Admittedly, the $FE^2$ is excessively costly if used to simulate macroscopic systems discretized with dense FE meshes. For this reason, practical applications of the method are pretty much limited, although extensive fundamental research has been conducted on this topic, see e.g. Coenen et al. (2012a, b), Feyel (1999, 2003), Feyel and Chaboche (2000), Geers et al. (2010), Kouznetsova et al. (2004a, b),

Kouznetsova and Geers (2008), Larsson and Runesson (2011), Miehe (1996), Miehe et al. (1999), Reis and Andrade Pires (2013), Temizer and Wriggers (2008, 2011), Werwer and Cornec (2000).

#### 3.3.1.2 Embedded Mean-Field Models

The macroscopic continuum-mechanics model model can use mean-field homogenization theories, in which the effective behavior of a polycrystal is used to derive its response, but the microstructure is represented in a statistical way. To this end, an aggregate of grains underlies every material point in the macro-scale model. Local macroscopic deformation is imposed on the aggregate, which causes changes in the orientation of the aggregate components. At the same time the averaged response of the aggregate defines the macroscopic behavior of the corresponding material point, thus deformation induced changes in plastic anisotropy is incorporated in the macroscopic finite element model. It has to be noted that we speak here of *direct embedding*, in which the crystal plasticity model is called during each increment of the macroscopic model and provides constitutive response.

Several embedded polycrystalline plasticity models were devised to describe the metal anisotropy in this way. The Taylor-type model (Asaro and Needleman 1985) was incorporated in works of Mathur and Dawson (1989, 1990) to simulate the evolution of crystallographic texture in Finite Element analysis of steady state forming simulations. The fully-implicit scheme based on the same Taylor-type model was later proposed in Kalidindi et al. (1992). Despite the relative simplicity of the Taylor assumption, this approach has proved to be quite predictive, as shown in by Jung et al. (2013), Kalidindi and Schoenfeld (2000), Schoenfeld (1998), to mention just a few examples. Yet from purely computational perspective, the models turned out to be costly, in particular if 3D macro-scale systems were simulated, which prompted research on accelerating the coupling. Massive parallel computing (e.g. Beaudoin et al. 1993; Mellbin et al. 2014) on one hand, and exploiting certain assumptions of the Taylor formulation[2] (see e.g. Zecevic et al. 2015a, b) on the other hand have served that purpose.

The mesoscopic viscoplastic self-consistent schemes have been successfully embedded into explicit time integration Finite Element codes. In particular, this coupling was tested on strongly anisotropic aggregates, such as hcp alloys in which plasticity at single-crystal level can be accommodated not only by slip but also by mechanical twinning (Tomé 2001; Walde and Riedel 2007a, b). This group of materials is particularly interesting, since such alloys typically develop pronounced crystallographic texture and rapidly evolve in terms of plastic anisotropy. The challenges to be addressed include rapid textural changes originating from twinning, and associated strong directional hardening/softening, as well as the highly anisotropic slip-twin interaction (Segurado et al. 2012). It is then argued that the

[2]See also Sect. 3.3.2.

fine-scale model has to be frequently queried for the homogenized response in order to accurately follow the microstructural changes.

Recently, several strategies of fully embedding the VPSC mean-field model also in the macroscopic implicit Finite Element analysis model have been proposed (Galán et al. 2014; Knezevic et al. 2013b, c; Segurado et al. 2012). Each integration point of the FE model is considered as a polycrystal that provides the stress and tangent stiffness matrix. The grain orientations approximate the initial texture, which may subsequently evolve with deformation. The strategies attempt to accelerate the calculations by extracting and reusing quantities that are computed as part of the nonlinear self-consistent homogenization scheme. For instance, the FE Jacobian matrix is expressed as a function of the viscoplastic tangent moduli, the elastic stiffness of the aggregate, and the FE time increment (Segurado et al. 2012).

Advanced coupling strategies have been developed to preserve fine-scale variables upon mesh adaptation in the FE macroscopic model, e.g. Prakash et al. (2015).

#### 3.3.1.3 Embedded Reduced Texture Models

Yet the number of the crystals associated to an individual integration point of a macroscopic FE mesh remains a hindering factor in terms of computational performance. To address this issue, an interesting concept to reduce the number of orientations per integration point was proposed by Raabe et al. (2004), Raabe and Roters (2004), Roters (2005), Zhao et al. (2004), where the authors suggested to de-associate the concepts of crystal and orientation and initially only consider some selected texture components. A similar idea was later elaborated in work (Knezevic and Landry 2015). The components are defined as compact functions, each characterized by its orientation (such as the ideal orientations: Goss, Brass or Cube component, etc.), a scatter around the orientation and the volume fraction of the component. The key concept is to exploit the fact that a huge number of crystals can be described by a single representative texture component. Since usually only a small number of texture components is present in a macrotexture, it is sufficient to map a relatively small number of ideal orientations to the macroscopic FE integration points. This is done in such a way that the superposition of all mapped components reproduce the initial texture of the material. However, during the simulation each of the mapped texture components undergoes its individual reorientation under local deformation conditions. Although the method allows reproducing the initial texture, it may not necessarily offer reliable predictions of the final texture at individual integration points. To understand why, let us suppose that just a single texture component is initially sufficient at a given integration point. If the component is unstable under a given deformation mode and, as a consequence, it breaks down into more than one component, the method will track just one of these evolved components and neglect all the others. On this basis, it is also doubtful whether local anisotropy can be accurately extracted from texture data that may become increasingly incomplete during the deformation.

As an alternative, the representative discrete orientations that are needed to reproduce the crystallographic texture can be spatially distributed over several neighboring integration points (Béringhier et al. 2007; Delannay et al. 2005; Logé and Chastel 2006). The way of distributing crystallographic orientations among the finite elements may be either proportional to the volume of the finite elements, or independent of it. In any case, the goal is obtain a good approximation of the ODF by merging contributions (discrete orientations) from several integration points. This way the ODF becomes a local material property of a group of several integration points, as opposed to fully embedded models that attempt to get the ODF locally approximated at every integration point.

## *3.3.2 Hierarchical Coupling*

### 3.3.2.1 Database and Sampling Techniques

A possible way to capture the influence of microstructural changes on the anisotropic response is to use a crystal plasticity model to calculate some homogenized quantities of interest in advance and later approximate these in a macroscopic simulation. This can be done by sampling followed by calculating a response surface, for instance by means of multivariate Kriging, as reported by Barton et al. (2008), Knap et al. (2008), Rouet-Leduc et al. (2014), or generalized in situ tabulation technique (Arsenlis et al. 2006). Alternatively, a sequence of explicit algebraic yield criteria can be pre-calculated for a finite set of strain levels and linearly interpolated during the macroscopic simulation (Knezevic et al. 2013b; Nixon et al. 2010a, b; Plunkett et al. 2006). In this case the database contains the parameters of the yield locus model expressed as a function of strain and possibly some other variables.

Since the exploited CP model is considered as a black box, the method can be virtually used with any CP model. However, the sampling is very expensive if it has to cover the evolution of the microstructural state variables in a multi-dimensional space. In practice, it is difficult to ascertain that the entire relevant part of that space is sufficiently probed. Nevertheless, it appears problematic that the local material state evolution may lead outside the validity range of the interpolation.

### 3.3.2.2 Spectral Crystal Plasticity (SCP)

The Spectral Crystal Plasticity (SCP) can be seen as a special case of database-type coupling. Whereas it also relies on sampling responses of a crystal plasticity framework, the way how the results are stored and queried greatly differentiates the SCP from the approach presented in the previous section. The database techniques store the homogenized responses of the RVE, while the SCP stores the intermediate results of a Taylor-type model.

Observe that if a Taylor-type model is used, each crystal is treated separately, and any per-grain solution of the crystal plasticity model depends solely on the orientation of the crystal and the strain rate imposed on it. The solution may include stress, lattice spin, shearing rates, Taylor factor etc. It is then possible to first evaluate a Taylor-type model for a large number of orientations and strain rates and subsequently store the results in an easily retrievable manner. As long as no other factors are taken into account, such as hardening of slip systems or grain interactions, these calculations can be done once and for all.

To achieve this, Fourier (spectral) representation of orientation distribution function (Bunge and Esling 1984) can be conveniently used for storing the results of a Taylor-type model, see Kalidindi and Duvvuru (2005), Kalidindi et al. (2006), Li et al. (2003), Van Houtte (2001). The one-time, but time consuming task is to find coefficients in Fourier series of the spectral representation for the functions that represent the per-grain solutions of the Taylor-type CP model. These solutions must be computed for each crystal orientation in Euler space subjected to all possible strain rates. This way, a database of spectral coefficients is generated. The advantage of the approach is that the result of the CP model can be later retrieved just by querying the database without doing any actual CP calculations.

The spectral method was first demonstrated using generalized spherical harmonics (GSH) (Kalidindi et al. 2006; Knezevic and Kalidindi 2007; Shaffer et al. 2010; Van Houtte 2001), and later employing Discrete Fourier Transforms (DFT) (Al-Harbi et al. 2010; Alharbi and Kalidindi 2015; Kalidindi et al. 2009; Knezevic et al. 2008, 2009). The DFT promises much higher computational performance since it exploits Fast Fourier Transform (FFTs) algorithm for fast retrieval of pre-computed crystal plasticity solutions. The solutions are stored on a uniform grid in the orientation space and subsequently a local spectral interpolation using Fast Fourier Transform is applied to recover the solutions for any orientation and deformation mode of interest (Knezevic et al. 2008).

A DFT-based SCP framework has been embedded into Finite Element model (Alharbi and Kalidindi 2015; Zecevic et al. 2015a, b). This is basically equivalent to embedding a Taylor-type model at each integration point of the FE model, however the constitutive response of the material can be evaluated much faster compared to a direct embedding scheme such as the CP-FEM.

The computational advantage of the SCP comes with certain drawbacks, though. Independent sampling of individual grains is implicitly required, thus the accuracy of the SCP is bound by the limitations of the Taylor assumptions. It is now well known that Taylor-type models do not offer best texture and anisotropy prediction. Furthermore, the SCP approach is hardly capable of going beyond quite simple Taylor-type models. For instance, adding internal variable hardening models would render the SCP impractical, since constructing the database of spectral coefficients would require exploring a high dimensional space.

### 3.3.3 Yield Criteria Based on Crystal Plasticity

As we have seen in the previous section, the direct coupling of microstructure evolution in a component-scale FE simulations is conceptually straightforward, but computationally complex. Therefore, more robust and efficient alternatives have been sought. It is quite easy to notice that the FE solver requires stress integration in the macroscopic domain, whereas the fine-scale crystal plasticity framework, if directly embedded, calculates much more than that.

This observation results in a concept to partly dissociate the evolution of properties and the evolution of the microstructure. To this end, the evolution of crystallographic texture and possibly other microstructural features are calculated by means of an appropriate crystal plasticity framework, but the macroscopic constitutive relation used in the FE only approximates the homogenized response of the fine-scale model. The microstructural evolution is directly implemented in this approach, since the orientations of the representative crystals and other microstructural state variables are updated according to the macroscopic plastic deformation. However, the mechanical description of the homogenized material response utilizes a different mathematical model, which can be efficiently plugged into the FE stress integration algorithm.

#### 3.3.3.1 Yield Criteria Defined by Interpolation

If a given deformation process is considered, the material is locally subjected to a certain stress state that slowly varies with increasing stain. Therefore, only a limited zone of the yield locus is probed by the stress integration algorithm. This was exploited by the works (Dawson et al. 2005; Duchêne et al. 2002; Habraken and Duchêne 2004), which proposed that the crystal plasticity yield locus is only sampled in a confined subspace of deviatoric stresses. Once the yield locus is locally known in a point-by-point manner, an interpolation method allows calculating a continuous function that approximates the yield locus. It needs to be emphasised that the interpolated yield locus is valid only within the range of the discrete set of known data points. When the available local description of the yield locus does not cover the region of interest anymore, one has to find another local description enclosing the new active part of the yield locus. The approach does neither explicitly enforce nor require any analytical yield locus model, since a generic interpolation scheme is sufficient. This has a drawback, though: the normals of locally interpolated yield loci may not be smooth, and thus stress integration that relies on the normality rule may experience convergence problems. Even though the interpolated function is continuously differentiable (e.g. $C^2$), there is still no guarantee that the interpolated yield locus is convex, with similar consequences as mentioned before.

#### 3.3.3.2 Yield Criteria Defined by Approximation

Recall from Chap. 1 that the phenomenological descriptions of plastic anisotropy have proved their enormous usefulness in modelling plastic anisotropy. Numerous successful efforts have been made in the last decades to improve the macroscopic anisotropy models, for example Aretz and Barlat (2012, 2013), Banabic et al. (2000, 2003, 2005, 2010), Barlat et al. (1991, 1997a, b, 2003b, 2005, 2007), Cazacu and Barlat (2004), Cazacu et al. (2006), Comsa and Banabic (2008), Hill (1948) Hosford (1979), Plunkett et al. (2006, 2008), Soare and Barlat (2010), Soare et al. (2008), Van Houtte and Van Bael (2004), Van Houtte et al. (2009), Vegter and van den Boogaard (2006), Vegter et al. (2003), Yoon et al. (2004, 2006, 2010, 2014), Yoshida et al. (2013). The improvements were attained not only in terms of predictive capabilities, but also with respect to computational performance. Due to these advantages, the phenomenological yield loci are nowadays most commonly adopted in commercial Finite Element (FE) packages dedicated for simulations of metal forming operations. If a yield locus model is used in a combination with flow theories, such as the normality flow theory, the phenomenological yield loci provide an efficient technique for capturing the effects of material anisotropy during the simulation of deformation processes. These advantages make the existing yield loci models perfect candidates for becoming components of a *hierarchical approach* that approximates the finer-scale model by a coarser-scale model.

The phenomenological yield criteria consider the polycrystalline material as homogeneous at the macroscopic level, and the yield surface depends merely on the macroscopic stress, strain rate, certain strain measures as well as their rates. The microstructural features of the material, such as crystallographic texture, can be indirectly taken into account by means of extensive parametrization of these models. The phenomenological yield loci are generally limited to the initial anisotropy of the material, since it is hardly possible to accurately predict the evolution of the yield surface without taking into account how the microstructure develops during the deformation. Usually it is assumed that the changes to the initial yield locus due to deformation are negligible. The assumption is approximately valid if the plastic strains are not excessively large, which admittedly holds in some sheet metal forming processes.

One can also find several examples that combine the strength of the two approaches: crystal plasticity frameworks and phenomenological yield loci mentioned above. The hierarchical multi-scale approach was followed, in which the fine-scale model provides data needed for identification of the macroscopic one that is based on a different mathematical framework. The yield criteria are given as parametrized closed-form functions. A least squares method can be then used to determine the parameters by fitting them to data points generated by virtual CP experiments. For instance, parameters of orthotropic Hill yield criterion can be easily derived by means of a Taylor-type model as shown in Kalidindi et al. (2004). Other phenomenological yield criteria have been also calibrated by means of the crystal plasticity frameworks, most remarkably FC Taylor, VPSC, ALAMEL and CP-FEM, see e.g. An et al. (2011), Barlat et al. (2005), Gawad et al. (2010, 2013),

Grytten et al. (2008), He et al. (2014), Inal et al. (2010), Kalidindi et al. (2004), Kim et al. (2007, 2008), Kraska et al. (2009), Plunkett et al. (2006), Saai et al. (2013), Savoie and MacEwen (1996), Van Bael et al. (2010), Van Houtte et al. (2009, 2011), Yoon et al. (2014), Zhang et al. (2014, 2015b).

Generally, to provide data for calibration, the crystal plasticity models have to be evaluated for a huge number of possible stress or strain rate modes, sometimes exceeding one million realizations. Given the fact that the number of parameters in the yield criteria is typically small, an overdetermined least squares approach was employed in some previous works, for instance in Grytten et al. (2008), Rabahallah et al. (2009) that focused on identifying the Yld2004 3D yield criterion (Barlat et al. 2005). However, indiscriminate selection of data points was typically used, which resulted in large data sets, varying in size from few thousands (Grytten et al. 2008; Zhang et al. 2015b) to tens of thousands of data points (Rabahallah et al. 2009).

This inspired works that aim at decreasing the computational effort related to evaluating necessary data points by running crystal plasticity virtual experiments. In order to maximize the amount of information acquired from every data point, not only the size of the yield locus, but also its curvature and derivatives can be simultaneously used (Gawad et al. 2010, 2013).

It has to be emphasized that the majority of the aforementioned efforts focuses on calibrating the initial yield locus, leaving the evolution of the plastic anisotropy unaddressed. The evolution of the yield locus can still be captured, though. If the strain path can be pre-determined, a sequence of explicit yield criteria can be pre-computed along that path for a finite set of strain levels and subsequently interpolated during the macroscopic FE simulation, as it was done in Knezevic et al. (2013b), Nixon et al. (2010a, b), Plunkett et al. (2006). Similarly as in the case of database and sampling techniques (see Sect. 3.3.2), the local deformation conditions in the FE mesh may fall outside the assumed deformation path, thus the evolution of the yield locus of may also lead outside the validity range of the interpolation.

Another viable method to tackle anisotropy evolution in the macroscopic FE problem is to use an adaptive hierarchical multi-scale approach. As opposed to the hierarchical methods outlined above, the adaptive scheme is capable of deriving macroscopic yield locus that reflects changes to the material along the actual deformation path. This can be expediently done by systematic updating of the material state, such as texture, by applying local macroscopic deformation rates and subsequent recalibration of the phenomenological plasticity model. Each Gauss integration point of a macroscopic FE mesh can be linked with an evolving yield locus function, as it was successfully demonstrated by Gawad et al. (2010, 2013), Van Bael et al. (2010), Van Houtte et al. (2011) using the Facet plastic potential (Van Houtte et al. 2009), and recently by He et al. (2014) that used the CPB06ex2 yield criterion (Cazacu et al. 2006). The evolution of the plastic anisotropy is therefore taken into account, as well as the evolution of the material state. In the next section we are going to closely examine a practical implementation of this concept.

#### 3.3.3.3 Evolving BBC2008 Yield Criterion

In this section we demonstrate how the adaptive hierarchical multi-scale approach can be utilized to model evolution of plastic anisotropy in a finite element simulation. For sake of simplicity, the texture is assumed to be the microstructural factor that primarily explains plastic anisotropy. A crystal plasticity framework will be then employed to predict changes in the crystallographic texture and to provide data needed for accommodating a macroscopic yield criterion in an adaptive manner. The yield criterion can be then incorporated into Finite Element model as a user-defined material model.

More specifically, we shall use an explicit time integration FEM, since this type of FE solvers is prevalently used in simulating sheet metal forming operations. For the same reason, elastic-plastic constitutive model will be assumed. The BBC2008 yield criterion will be calibrated by virtual experiments conducted by means of the ALAMEL crystal plasticity model.

We shall begin with a notion that material properties may evolve independently within small volumes of material, typically in individual finite elements. To achieve that, each integration point in the macroscopic mesh is associated with a collection of state variables:

**macroscopic state variables** (denoted as $\mathbf{Z}$) that comprise a parametric yield locus function (along with a current set of parameters). Additionally, control variables are included that decide when and how the yield locus function should be reconstructed.
**microscopic state variables** (denoted as $\mathbf{z}$) consist of variables that are relevant to the crystal plasticity framework. The state variables must be sufficient to construct an RVE. In our case, the variables in $\mathbf{z}$ are limited to the Orientation Distribution Function given in a discrete form, i.e. as a list of crystal orientations associated with their relative volume fractions. Although in the currently presented case the texture is the only micro-scale state variable, other microstructural features can be added, so the material would be described in a much more extensive way if the CP model permits so. For instance, $\mathbf{z}$ can be enriched by including phase composition, grain size and shape, ODF and/or MODF of individual phases, resistance of available deformation mechanisms (slip and twinning systems), substructure (dislocation densities or patterns), and many others.

Of course, the macroscopic state variables must include the stress state at the integration point and a local measure of plastic strain, both needed by the stress integration algorithm. The details of incorporating the yield criterion as such into the elastic-plastic explicit time integration FE are skipped here, since they are not essential in the presented method. The reader may refer to Chap. 1 for examples how this can be achieved in the context of implicit or explicit time integration FE codes. We have to mention however that the presented multi-scale model makes the assumption that a macroscopic hardening model is available in the FE code.

If an explicit time integration FE solver is used, the total deformation is subdivided into many small time increments, satisfying the stability conditions of the time integration scheme. It is quite obvious that recalculations of the parameters of the yield criterion at each integration point in every time increment would be highly inefficient. Given small strains associated to the time increments, one may postpone updating the state variables $\mathbf{z}$ and the subsequent recalculation of $\mathbf{Z}$ until a certain criterion is met at the considered integration point.

A possible criterion, as proposed in Gawad et al. (2013), is based on tracking the plastic strain accumulated since the previous update of the anisotropy model. The accumulated plastic strain is calculated by integrating instantaneous plastic strain rate $\mathbf{D}$ over time increments as

$$\mathbf{P} = \int_{t_{i-1}}^{t_i} \mathbf{D}(t)\,\mathrm{d}t \tag{3.1}$$

where $t_i$ is the current time since the start of the simulation, and $t_{i-1}$ is the time of the previous update. This quantity is used as the control variable in making decision if $\mathbf{Z}$ needs to be updated. The criterion is fulfilled if

$$\|\mathbf{P}\| \geq P_{cr} \tag{3.2}$$

where $P_{cr}$ is a control parameter interpreted as a critical value to trigger the update. Again, we emphasize that the tracking is carried out independently at each integration point. Similarly, the decision about the update is made independently from one integration point to another.

Once the criterion is satisfied, both the microstructural state variables and the anisotropy model at the integration point are updated. To do so, three steps are taken:

1. evolution of $\mathbf{z}$ along the recent deformation path $\mathbf{P}$ is calculated by the crystal plasticity model,
2. necessary crystal plasticity virtual experiments are conducted to characterize the material in its updated state, and finally
3. a new vector of yield locus parameters coefficients in $\mathbf{Z}$ is computed to fit the results of the virtual experiments.

In the next paragraphs we will reiterate over these steps, however they will be presented in a slightly different order.

**Macroscopic yield locus** Chap. 1 provides several examples of yield loci, which vary with respect to their capability to describe plastic anisotropy of the material. The formulae presented there are typically used to describe the initial yield locus or the yield locus that corresponds to a small level of plastic strain. Let us use as an example the BBC2008 plane stress yield criterion, which was originally proposed by Comsa and Banabic (2008). The formulae of the BBC2008 yield criterion can be found in Chap. 1. To exploit the plane stress yield locus, we make a constitutive assumption

that the macroscopic material is a plastically orthotropic membrane under plane-stress conditions. Given the plane-stress constraint, the only non-zero components of the Cauchy stress tensor $\boldsymbol{\sigma}$ are $\sigma_{11}$, $\sigma_{22}$ and $\sigma_{12} = \sigma_{21}$. Notwithstanding, the plane stress assumption and its consequences are not mandatory and the coupling scheme can be easily generalized to full 3D tensors, as shown in Gawad et al. (2013).

Recall from Chap. 1 that in order to distinguish whether the material is deformed elastically or plastically, a scalar-valued yield function is usually defined:

$$F(\boldsymbol{\sigma}) = \bar{\sigma}(\boldsymbol{\sigma}) - Y \leq 0 \tag{3.3}$$

where $\bar{\boldsymbol{\sigma}} \geq 0$ is the equivalent yield stress and $Y > 0$ is an arbitrary reference yield stress. The function $F$ describes the yield locus or, more specifically, the shape and size of the yield surface. The yield surface holds the property that $F(\boldsymbol{\sigma}) = 0$ when the deformation occurs elasto-plastically, whereas purely elastic stress state satisfies the strict inequality $F(\boldsymbol{\sigma}) < 0$.

The formalism used in (3.3) does not explicitly account for the influence of the material state on plastic anisotropy, not to mention the impact of the microstructural state variables. Let $\mathbf{z}$ denote the instantaneous material state variables that in our case specifically include texture of the material. We assume that the state variables evolve as

$$\mathbf{z} = \mathbf{z}(\varepsilon_{pl}) \tag{3.4}$$

Apart from the dependency on plastic strain $\varepsilon_{pl}$, the state variables may also be expressed as depending on a combination of time, temperature, plastic work and possibly other variables. The evolution equation of $\mathbf{z}$ is rarely given in a closed form. In fact, in most cases the evolution of the microscopic state variables is only known from a simulation.

An extension to the yield criterion can be introduced by adding parameters that depend on $\mathbf{z}$:

$$F(\boldsymbol{\sigma}, \mathbf{z}) = \bar{\sigma}(\boldsymbol{\sigma}, \mathbf{z}) - Y \leq 0 \tag{3.5}$$

Therefore, the extended form (3.5) also discards the assumption that the plastic anisotropy does not change during the plastic deformation. Let us now re-write the formulae of the BBC2008 yield criterion using the formalism provided by Eq. (3.5).

The BBC2008 yield criterion defines the equivalent stress as:

$$\bar{\sigma}(\boldsymbol{\sigma}, \mathbf{z}) = \left[ (w-1) \sum_{i=1}^{s} \{ w^{i-1} P(\boldsymbol{\sigma}, \mathbf{z}) + w^{s-1} Q(\boldsymbol{\sigma}, \mathbf{z}) \} \right]^{\frac{1}{2k}} \tag{3.6}$$

$$P(\boldsymbol{\sigma}, \mathbf{z}) = \left[ L^{(i)}(\boldsymbol{\sigma}, \mathbf{z}) + M^{(i)}(\boldsymbol{\sigma}, \mathbf{z}) \right]^{2k} + \left[ L^{(i)}(\boldsymbol{\sigma}, \mathbf{z}) - M^{(i)}(\boldsymbol{\sigma}, \mathbf{z}) \right]^{2k} \tag{3.7}$$

$$Q(\boldsymbol{\sigma},\mathbf{z}) = \left[M^{(i)}(\boldsymbol{\sigma},\mathbf{z}) + N^{(i)}(\boldsymbol{\sigma},\mathbf{z})\right]^{2k} + \left[M^{(i)}(\boldsymbol{\sigma},\mathbf{z}) - N^{(i)}(\boldsymbol{\sigma},\mathbf{z})\right]^{2k} \tag{3.8}$$

The coefficient $w$ is defined as $w = (3/2)^{1/s} > 1$, where $s \in \mathbb{N}$. The choice of the exponent $k$ must satisfy the condition that $s \in \mathbb{N}$ to ensure convexity of the yield surface (Comsa and Banabic 2008). Furthermore, Comsa and Banabic (2008) recommended to use $k = 4$ and $k = 3$ for fcc and bcc materials, respectively. The scalar functions $L$, $M$ and $N$ are given by:

$$L^{(i)}(\boldsymbol{\sigma},\mathbf{z}) = L^{(i)}(\sigma_{11},\sigma_{22},\mathbf{z}) = l_1^{(i)}(\mathbf{z})\sigma_{11} + l_2^{(i)}(\mathbf{z})\sigma_{22} \tag{3.9}$$

$$\begin{aligned} M^{(i)}(\boldsymbol{\sigma},\mathbf{z}) &= M^{(i)}(\sigma_{11},\sigma_{22},\sigma_{12},\mathbf{z}) \\ &= \sqrt{\left[m_1^{(i)}(\mathbf{z})\sigma_{11} - m_2^{(i)}(\mathbf{z})\sigma_{22}\right]^2 + \left[m_3^{(i)}(\mathbf{z})(\sigma_{12}+\sigma_{21})\right]^2} \end{aligned} \tag{3.10}$$

$$\begin{aligned} N^{(i)}(\boldsymbol{\sigma},\mathbf{z}) &= N^{(i)}(\sigma_{11},\sigma_{22},\sigma_{12},\mathbf{z}) \\ &= \sqrt{\left[n_1^{(i)}(\mathbf{z})\sigma_{11} - n_2^{(i)}(\mathbf{z})\sigma_{22}\right]^2 + \left[n_3^{(i)}(\mathbf{z})(\sigma_{12}+\sigma_{21})\right]^2} \end{aligned} \tag{3.11}$$

Equations (3.9)–(3.11) contain several parameters that depend on the material state $\mathbf{z}$. These parameters can be conveniently gathered into the vector:

$$\mathbf{p} = \{l_1^{(i)}(\mathbf{z}), l_2^{(i)}(\mathbf{z}), m_1^{(i)}(\mathbf{z}), m_2^{(i)}(\mathbf{z}), m_3^{(i)}(\mathbf{z}), n_1^{(i)}(\mathbf{z}), n_2^{(i)}(\mathbf{z}), n_3^{(i)}(\mathbf{z})\ (i = 1,\ldots,s)\} \tag{3.12}$$

Depending on the parameter $s$, the BBC2008 yield criterion may include 8 components in $\mathbf{p}$ for $s = 1$, 16 components if $s = 2$, 24 components for $s = 3$ and so forth. To simplify the notation, BBC2008p$N$ stands for the BBC2008 yield criterion comprising $N$ parameters. To determine $N$ parameters, at least the same number of data points has to be provided by means of crystal plasticity virtual experiments. We emphasize this experimental nature (even though the experiments are virtual) by marking the data points with the superscript '(exp)'.

In Chap. 1 we presented an extensive calibration procedure that allows one to use arbitrary points of the plane stress yield locus. To recapitulate the most important points, the identification problem is posed as minimisation of square norm of the vector-valued error function:

$$\mathbf{E}(\mathbf{p}) = \begin{Bmatrix} w_y\mathbf{y}(\mathbf{p}) \\ w_r\mathbf{r}(\mathbf{p}) \\ w_{yb}\mathbf{y}_b(\mathbf{p}) \\ w_{rb}\mathbf{r}_b(\mathbf{p}) \\ w_S\mathbf{S}(\mathbf{p}) \\ w_\beta\boldsymbol{\beta}(\mathbf{p}) \end{Bmatrix} \tag{3.13}$$

where

$$\mathbf{y}(\mathbf{p}) = \left\{1 - \frac{y(\mathbf{p}, \alpha_1)}{y^{(\exp)}(\alpha_1)}, \ldots, 1 - \frac{y(\mathbf{p}, \alpha_n)}{y^{(\exp)}(\alpha_n)}\right\}^T \tag{3.14}$$

$$\mathbf{r}(\mathbf{p}) = \left\{1 - \frac{r(\mathbf{p}, \alpha_1)}{r^{(\exp)}(\alpha_1)}, \ldots, 1 - \frac{r(\mathbf{p}, \alpha_n)}{r^{(\exp)}(\alpha_n)}\right\}^T \tag{3.15}$$

$$\mathbf{y}_b(\mathbf{p}) = \left\{1 - \frac{y_b(\mathbf{p})}{y_b^{(\exp)}}\right\}^T \tag{3.16}$$

$$\mathbf{r}_b(\mathbf{p}) = \left\{1 - \frac{r_b(\mathbf{p})}{r_b^{(\exp)}}\right\}^T \tag{3.17}$$

$$\mathbf{S}(\mathbf{p}) = \left\{1 - \frac{S(\mathbf{p}, \theta_1)}{S^{(\exp)}(\theta_1)}, \ldots, 1 - \frac{S(\mathbf{p}, \theta_m)}{S^{(\exp)}(\theta_m)}\right\}^T \tag{3.18}$$

$$\boldsymbol{\beta}(\mathbf{p}) = \left\{\cos\left(\beta^{(\exp)}(\theta_1) - \beta_1(\mathbf{p}, \theta_1)\right), \ldots, \cos\left(\beta^{(\exp)}(\theta_m) - \beta_m(\mathbf{p}, \theta_m)\right)\right\}^T \tag{3.19}$$

The components of vectors $\mathbf{y}(\mathbf{p})$ and $\mathbf{r}(\mathbf{p})$ include residuals pertaining to the series of $n$ uniaxial tensile tests along angles $\alpha_i$ w.r.t. RD. Uniaxial yield stress $y^{(\exp)}(\alpha)$ and $y(\mathbf{p}, \alpha)$ are calculated in the direction $\alpha$ by the CP virtual experiments and derived from the yield criterion (3.6), respectively, while $r^{(\exp)}(\alpha)$ and $r(\mathbf{p}, \alpha)$ are the $r$-values obtained in analogous way. The contribution of the equibiaxial point to the error function is included via terms (3.16) and (3.17). Other points that lie on the $\sigma_{11}$ and $\sigma_{22}$ section are indicated by the angle $\theta$, which defines the ratio between $\sigma_{11}$ and $\sigma_{22}$: $\tan\theta = \frac{\sigma_{22}}{\sigma_{11}}$. The contribution (3.18) provides the magnitude of the yield stress $S(\mathbf{p}, \theta)$ in the direction given by the angle $\theta$. The normal to the yield contour and the $\sigma_{11}$ direction form the angle $\beta(\theta)$. The weighting factors $w_y$, $w_r$, $w_{yb}$, $w_{rb}$, $w_S$ and $w_\beta$ allow one to control the relative importance of the individual components of the error function. This minimization problem can be conveniently solved by means of general non-linear least squares solvers, such as the Levenberg-Marquardt or the Trust Region algorithms (Conn et al. 2000).

**Crystal Plasticity Virtual Experiments** The data needed by (3.18) and (3.19) can be calculated by the crystal plasticity framework, which accounts for the evolution of fine-scale material state $\mathbf{z}$.

At this moment we assume that the CP framework can be seen as a black box that provides:

- homogenized stress $\sigma(\mathbf{D}, \mathbf{z})$,
- evolution of $\mathbf{z}$.

As a matter of fact, many crystal plasticity models are *strain rate driven*, similarly as the black box mentioned above. The homogenized stresses calculated by the black box can be seen as evaluations of function $f$: $\sigma_H(\dot{\varepsilon}, \mathbf{z}) = f(\dot{\varepsilon}, \mathbf{z})$, even though $f$ is not given in a closed form. However, in many deformation processes it is the stress state that is either known or assumed by certain idealization. In such case the crystal plasticity model would need to predict what macroscopic deformation might be reached under a superimposed macroscopic stress $\boldsymbol{\sigma}$. This also poses certain inconveniences in (3.13). On one hand, the components of the residual vector (3.13) are expressed as stress-state dependent. On the other hand, the opaque nature of a black box does not permit any direct inversion of the function it provides. For these reasons, a numerical inversion of $f$ must be employed. An iterative procedure can be then employed to to analyze deformation paths defined by macroscopic stress modes, even though a strain-rate driven crystal plasticity model is used. Note that the homogenization scheme in the CP model does not require imposing stress boundary condition on every individual grain, and therefore it is not necessarily satisfied on the grain level.

An iterative procedure can be then employed to analyze deformation paths defined by macroscopic stress modes, even though a strain-rate driven crystal plasticity model is used. Again, it has to be remarked that the homogenization scheme does not require imposing stress boundary condition on every individual grain, and therefore it is not necessarily satisfied on the grain level. On the grain level Eqs. (3.39)–(3.50) still hold and the microscopic boundary conditions are defined in terms of the velocity gradient. The crystal plasticity model is then considered as a black-box implementing a purely plastic rate-insensitive material. It must allow evaluating the homogenized macroscopic deviatoric stress $\mathbf{S}_H$ as a response to the macroscopic plastic strain rate $\mathbf{D}$, while keeping the state variables unmodified. An update of the state variables can be independently requested from the black-box.

Since the underlying crystal plasticity model neglects the elastic components of stress and strain rate, the homogenized stress is inherently deviatoric and the corresponding macroscopic strain rate has to satisfy the volumetric incompressibility condition. Therefore, any of these tensor quantities contains only five independent components, which can be utilized by converting the second-order tensor quantities of deviatoric nature into five-dimensional vectors. In this context the primary reason for preferring the five-dimensional vector representation is that the conversion allows one to reduce the dimensionality of the search space, since the constraint $\operatorname{tr} \mathbf{x} = 0$ is automatically satisfied by the five-dimensional vector representation.

One can conveniently reduce the dimensionality of the search space by exploiting the fact that symmetric second-order tensors of deviatoric nature contain only five independent components. This property is commonly found in tensors used in mechanics; for instance, deviatoric stresses and plastic strain rates belong to this category. The reduction of dimensionality can be done by converting

appropriate tensors into five-dimensional vectors, e.g. by following the transformation proposed in Van Houtte and Van Bael (2004). Other variants of the transformation exist in the literature, see e.g. Grytten et al. (2008), Lequeu et al. (1987), Van Houtte (1988). Throughout the remaining part of the paper the convention will be used that $\hat{\mathbf{x}}$ denotes vector representation of rank-two tensor $\mathbf{x}$.

Let $\mathbf{x}$ be a symmetric, second-order tensor that has the property that $\mathbf{x}_{11} + \mathbf{x}_{22} + \mathbf{x}_{33} = 0$. It can be then completely described by only five independent components. According to Van Houtte and Van Bael (2004), the components of the corresponding 5D vector $\hat{\mathbf{x}}$ can be calculated as:

$$\hat{\mathbf{x}}_1 = \frac{1}{\sqrt{2}}(\mathbf{x}_{11} - \mathbf{x}_{22}) \tag{3.20}$$

$$\hat{\mathbf{x}}_2 = -\sqrt{\frac{3}{2}}\mathbf{x}_{33} \tag{3.21}$$

$$\hat{\mathbf{x}}_3 = \sqrt{2}\mathbf{x}_{23} \tag{3.22}$$

$$\hat{\mathbf{x}}_4 = \sqrt{2}\mathbf{x}_{31} \tag{3.23}$$

$$\hat{\mathbf{x}}_5 = \sqrt{2}\mathbf{x}_{12} \tag{3.24}$$

It is trivial to convert back the 5D vector into the second-order tensor:

$$\mathbf{x}_{11} = \frac{1}{\sqrt{2}}\hat{\mathbf{x}}_1 + \frac{1}{\sqrt{6}}\hat{\mathbf{x}}_2 \tag{3.25}$$

$$\mathbf{x}_{22} = -\frac{1}{\sqrt{2}}\hat{\mathbf{x}}_1 + \frac{1}{\sqrt{6}}\hat{\mathbf{x}}_2 \tag{3.26}$$

$$\mathbf{x}_{33} = -\sqrt{\frac{2}{3}}\hat{\mathbf{x}}_2 \tag{3.27}$$

$$\mathbf{x}_{23} = \mathbf{x}_{32} = \frac{1}{\sqrt{2}}\hat{\mathbf{x}}_3 \tag{3.28}$$

$$\mathbf{x}_{31} = \mathbf{x}_{13} = \frac{1}{\sqrt{2}}\hat{\mathbf{x}}_4 \tag{3.29}$$

$$\mathbf{x}_{12} = \mathbf{x}_{21} = \frac{1}{\sqrt{2}}\hat{\mathbf{x}}_5 \tag{3.30}$$

It can be easily shown that the scalar product is preserved, i.e. $\mathbf{x} : \mathbf{x} = \hat{\mathbf{x}} \cdot \hat{\mathbf{y}}$. As a corollary, the length of the vector $\hat{\mathbf{x}}$ is equal to the magnitude of the corresponding tensor $\mathbf{x}$.

The 5D representation of plastic strain rate and deviatoric stress is used in the inversion of the function $\sigma(\dot{\varepsilon}, \mathbf{z}) = f(\dot{\varepsilon}, \mathbf{z})$.

Algorithm 1 is able to deliver $m$ data points corresponding to biaxial stress state with arbitrary stress ratios.

The fundamental part of the algorithm is to find the macroscopic plastic strain rate mode $\hat{\mathbf{A}}^*$ that corresponds to the imposed deviatoric stress mode $\hat{\mathbf{U}}^*$, where

$$\hat{\mathbf{U}} = \frac{\hat{\mathbf{S}}}{\|\hat{\mathbf{S}}\|} \tag{3.31}$$

and $\hat{\mathbf{S}}$ is a five-dimensional vector representing the deviatoric part of the stress tensor $\boldsymbol{\sigma}$ that defines the requested deformation path:

$$\mathbf{S} = \boldsymbol{\sigma} - \frac{\operatorname{tr}\boldsymbol{\sigma}}{3}\mathbf{I} \tag{3.32}$$

where $\mathbf{I}$ is the identity tensor. This is achieved by solving an unconstrained optimization problem, in which the square norm of the vector-valued residual function

$$\mathbf{f}(\hat{\mathbf{A}}, \hat{\mathbf{U}}^*) = \hat{\mathbf{U}}^* - \frac{\hat{\mathbf{S}}_H(\hat{\mathbf{A}})}{\|\hat{\mathbf{S}}_H(\hat{\mathbf{A}})\|} \tag{3.33}$$

is minimized. In the subsequent derivations a simplified notation will be used: $\mathbf{f}(\hat{\mathbf{A}}, \hat{\mathbf{U}}^*) = \mathbf{f}(\hat{\mathbf{A}})$, since the imposed stress mode is considered a constant. The evaluation of the residual function involves a call to the underlying crystal plasticity to calculate the homogenized stress $\mathbf{s}_H$. The search starts from an initial guess $\hat{\mathbf{A}}_0$, typically chosen as $\hat{\mathbf{A}}_0 = \hat{\mathbf{U}}^*$, which corresponds to the property of an isotropic von Mises plastic material. From a current point $\hat{\mathbf{A}}_{\text{old}}$, the algorithm iteratively uses the trust-region minimization approach (Conn et al. 2000)

$$\min_{\hat{\mathbf{A}} \in \mathbb{R}^5} \|\mathbf{f}(\hat{\mathbf{A}}_{\text{old}}) + \mathbf{J}(\hat{\mathbf{A}}_{\text{old}})\left(\hat{\mathbf{A}}_{\text{new}} - \hat{\mathbf{A}}_{\text{new}}\right)\| \quad \text{subject to} \quad \|\hat{\mathbf{A}}_{\text{new}} - \hat{\mathbf{A}}_{\text{old}}\| \leq \delta \tag{3.34}$$

to find a new guess $\hat{\mathbf{A}}_{\text{new}} = \hat{\mathbf{A}}_{\text{old}} + \Delta\hat{\mathbf{A}}$ that satisfies

$$\min_{\hat{\mathbf{A}} \in \mathbb{R}^5} \|\mathbf{J}^T(\hat{\mathbf{A}})\mathbf{J}(\hat{\mathbf{A}})\Delta\hat{\mathbf{A}} + \mathbf{J}(\hat{\mathbf{A}})\mathbf{f}(\hat{\mathbf{A}})\| \tag{3.35}$$

where $\Delta\hat{\mathbf{A}}$ is the trial step, $\delta$ is the size of the trial step and $\mathbf{J}$ is the Jacobian matrix of the function $\mathbf{f}$. The search is terminated when any of the following criteria is fulfilled:

- $\|\mathbf{f}(\hat{\mathbf{A}}_{\text{new}})\|$ is smaller than a pre-defined threshold $f_{\text{tol}}$, or
- $\|\Delta\hat{\mathbf{A}}\|$ is smaller than a pre-defined minimal step size, or
- the number of iterations exceeds its maximal value.

As can be seen from Eqs. (3.34) and (3.35), the Jacobian matrix has to be calculated very often. Since it is not available in a closed form, one has to compute it numerically by a finite difference scheme, which is associated with a considerable cost. However, if the initial guess $\hat{\mathbf{A}}_0$ is sufficiently close to the solution, one may attempt to locate the minimum under the auxiliary assumption that $\mathbf{J}(\hat{\mathbf{A}}) = \mathbf{J}(\hat{\mathbf{A}}_0) = const$. From this assumption it follows that the linearized problem is solved, so (3.34) and (3.35) become:

$$\min_{\hat{\mathbf{A}}\in\mathbb{R}^5} \|\mathbf{f}(\hat{\mathbf{A}}_{\text{old}}) + \mathbf{J}(\hat{\mathbf{A}}_0)\left(\hat{\mathbf{A}}_{\text{new}} - \hat{\mathbf{A}}_{\text{new}}\right)\| \quad \text{subject to} \quad \|\hat{\mathbf{A}}_{\text{new}} - \hat{\mathbf{A}}_{\text{old}}\| \leq \delta \tag{3.36}$$

$$\min_{\hat{\mathbf{A}}\in\mathbb{R}^5} \|\mathbf{J}^T(\hat{\mathbf{A}}_0)\mathbf{J}(\hat{\mathbf{A}}_0)\Delta\hat{\mathbf{A}} + \mathbf{J}(\hat{\mathbf{A}}_0)\mathbf{f}(\hat{\mathbf{A}})\| \tag{3.37}$$

where the matrix product $\mathbf{J}^T(\hat{\mathbf{A}}_0)\mathbf{J}(\hat{\mathbf{A}}_0)$ can be conveniently pre-calculated. If the trust region algorithm fails to converge to an acceptable solution, one may drop the assumption on constant Jacobian and restart the minimization from the initial guess.

Incidentally, in many cases there is a sufficiently accurate initial guess available. For instance, it may be obtained from a previous run of the method that had explored a similar stress mode, which holds as long as an identical material state was used by the underlying crystal plasticity model. Such condition is frequently fulfilled if one systematically calculates a point-by-point yield locus section (for instance, the section defined by $\sigma_{11} - \sigma_{22}$ plane). Yet another example is that the initial guess may be provided by an analytical yield locus model calibrated for a very similar material state.

The generic procedure outlined above can be straightforwardly utilized for determining data points that are commonly used in calibration of analytical yield loci. The authors have implemented it in a set of algorithms, collectively known as the Virtual Experimentation Framework (VEF) that allows conducting crystal plasticity virtual experiments either in stress or strain rate driven mode. For instance, uniaxial tension, uniaxial compression and biaxial stress state can be studied by means of the VEF. Suppose that the material state variables, such as texture, are expressed in a reference frame defined by the $\mathbf{e}_1, \mathbf{e}_2, \mathbf{e}_3$ directions. In many practical applications these directions coincide with the rolling direction (RD), transverse direction (TD) and normal direction (ND). Algorithm 2 allows calculating instantaneous $r$-values and corresponding yield stresses for a sequence of angles defining rotation around $\mathbf{e}_3$ from the $\mathbf{e}_1$ axis.

A similar algorithm (see Algorithm 3) can be used for calculating evolution of the material state under the stress mode $\hat{\mathbf{U}}^*$. The algorithm provides a convenient way to determine whether the microscopic state (e.g. crystallographic texture) is stable under the imposed stress mode and to estimate how the associated strain rate

evolves. In principle, the algorithm splits the deformation path into smaller increments of plastic strain which results from the stress mode $\mathbf{U}^*$, given the microstructural state of the material. The size of increments is specified by the input parameter $\Delta\varepsilon$. At the end of each increment the state of the microstructure is updated to reflect the changes caused by the deformation. Eventually the procedure returns a sequence of triplets $(\varepsilon, \mathbf{A}, \mathbf{S}_H(\mathbf{A}))$. Non-essential operations, such as reporting the history of microstructural state variables, are omitted for clarity.

Suppose one wants to determine the contour of the yield locus. Algorithm 1 presents how the normalized $\sigma_{11}, \sigma_{22}$ yield locus section can be calculated. The algorithm can be also used for collecting data needed for calculating the Cartesian tangent to the yield locus contour:

$$\frac{d\sigma_{22}}{d\sigma_{11}} = \frac{\frac{dS(\theta)}{d\theta}\sin\theta + S(\theta)\cos\theta}{\frac{dS(\theta)}{d\theta}\cos\theta - S(\theta)\sin\theta} \tag{3.38}$$

where $S(\theta)$ is the distance from the origin of the coordinate system to the yield locus contour in that section. The polar derivative $\frac{dS(\theta)}{d\theta}$ can be numerically estimated from a single run of Algorithm 1.

**Crystal plasticity ALAMEL** In the previous paragraph we considered the crystal plasticity model as a generic black box. Let us now consider a specific CP framework, namely the rate-independent ALAMEL model proposed by Van Houtte et al. (2005). As mentioned in Sect. 3.2.1, the ALAMEL belongs to the family of statistical grain interaction models. The reader is referred to the paper (Van Houtte et al. 2005), which provides a comprehensive discussion of the statistical crystal plasticity theories relevant to this work, including foundations of Taylor's theory.

This section briefly summarizes basic concepts of the ALAMEL model. Since the remaining part of the work concentrates mostly on mechanical aspects, such as yielding, the discussion of texture evolution is much limited for brevity. Let us now just mention that the ALAMEL crystal plasticity model deals with an aggregate of grains (a polycrystal). Each grain is characterized by its orientation assigned from the Orientation Distribution Function (ODF) $f(g)$ where $g \in \mathcal{R}^3$ represents the crystal orientation. The whole aggregate of grains thus corresponds to a discrete form of the ODF $f_d(g)$. The slips on individual slip systems cause rotations of the grains, and as a result evolution of texture, which is the primary component of micro-scale state $\mathbf{z}$. More details on how the lattice rotations are related to the crystallographic slip can be found in Chap. 2.

A macroscopic deformation may be imposed onto an aggregate of crystals by specifying the velocity gradient $\mathbf{L}$. This velocity gradient tensor can be additively decomposed into a symmetric part $\mathbf{D}$, which is the plastic strain rate, and anti-symmetric part $\mathbf{W}$:

**Algorithm 1:** VEF algorithm for calculating scaled $\sigma_{11}, \sigma_{22}$ yield locus section

**Input**: angular range: $\theta_0$, $\theta_{\max}$, angular resolution: $\Delta\theta$, scaling stress: $S_s$, shear stress: $\sigma_{12}$, logical flag: $reusePrevious$

**Result**: sequence of pairs $(\theta, S(\theta)/S_s)$: $\mathbf{o}$

$\mathbf{o} \leftarrow \emptyset$

**for** $\theta = \theta_0$ *to* $\theta_{\max}$ *every* $\Delta\theta$ **do**

$\boldsymbol{\sigma} \leftarrow \begin{bmatrix} \cos\theta & \sigma_{12} & 0 \\ \sigma_{12} & \sin\theta & 0 \\ 0 & 0 & 0 \end{bmatrix}$

$\mathbf{S} \leftarrow \boldsymbol{\sigma} - \frac{1}{3}\mathrm{tr}\,\boldsymbol{\sigma}\,\mathbf{I}$

$\mathbf{U}^* \leftarrow \dfrac{\mathbf{S}}{\|\mathbf{S}\|}$

**if** $\theta \neq \theta_0$ *and reusePrevious* **then** $\hat{\mathbf{A}}_0 \leftarrow \hat{\mathbf{A}}^*$

$\hat{\mathbf{A}}^* \leftarrow \underset{\hat{\mathbf{A}} \in \mathbb{R}^5}{\mathrm{argmin}} \|\mathbf{F}(\hat{\mathbf{A}}, \hat{\mathbf{U}}^*)\|$ given $\hat{\mathbf{A}}_0$ `// see (3.33)-(3.37)`

$S \leftarrow \|\mathbf{S}_H(\mathbf{A}^*)\|$

$\mathbf{o} \leftarrow \mathbf{o} + (\theta, \dfrac{S}{S_s})$ `// extend the sequence o`

**end**

$$\mathbf{L} = \mathbf{D} + \mathbf{W} \tag{3.39}$$

Let us first consider a single-phase polycrystalline aggregate, consisting of a number of grains. In the Taylor-type models, it is supposed that each grain has homogeneous properties, such as crystal orientation, as well as homogeneous stress and strain distributions over the volume. If a single grain is considered, a local constitutive law has to establish relations between the local stress, strain and rigid body rotation inside the volume of the grain. A crystal plasticity theory, for instance the Generalized Schmid Law, allows one to account for internal processes, such as slip on various slip systems and the rotation of the crystal lattice, which occur as a response to the external stimuli.

Suppose the local velocity gradient $\mathbf{l}$ is imposed on a single grain. Additive decomposition of the velocity gradient tensor leads to

$$\mathbf{l} = \mathbf{d} + \mathbf{w} \tag{3.40}$$

where the symmetric part $\mathbf{d}$ is referred to as the local strain rate, and the anti-symmetric part $\mathbf{w}$ is called the local spin. Provided that elasticity is neglected, the strain rate needs to be accommodated through plastic deformation, which is carried by dislocation slip on a number of slip systems and/or by twinning on twinning systems. The further discussion is confined to the plastic slip as the only mechanism of plastic deformation.

**Algorithm 2:** VEF algorithm for calculating $r$-values and normalized yield stresses for a sequence of uniaxial loadings defined by directions $\boldsymbol{\alpha}$

**Input**: sequence of angles: $\boldsymbol{\alpha} = [\alpha_1, \ldots, \alpha_n]$, stress state: $m$ (either 1 for tension or -1 for compression), accuracy threshold: $f_{\text{tol}}$, logical flag: *reusePrevious*

**Result**: sequence of triplets $(\alpha, r_\alpha, y_\alpha)$: $\mathbf{o}$

$\boldsymbol{\sigma}_0 \leftarrow m \begin{bmatrix} 1 & 0 & 0 \\ 0 & 0 & 0 \\ 0 & 0 & 0 \end{bmatrix}$

$\mathbf{o} \leftarrow \emptyset$

*hasConverged* $\leftarrow$ False

**foreach** $\alpha$ *in* $\boldsymbol{\alpha}$ **do**

  $\mathbf{R} \leftarrow \begin{bmatrix} \cos\alpha & -\sin\alpha & 0 \\ \sin\alpha & \cos\alpha & 0 \\ 0 & 0 & 1 \end{bmatrix}$ `// Rotation matrix`

  $\boldsymbol{\sigma}_r \leftarrow \mathbf{R}^T \boldsymbol{\sigma}_0 \mathbf{R}$

  $\mathbf{S}_r \leftarrow \boldsymbol{\sigma}_r - \frac{1}{3} \operatorname{tr} \boldsymbol{\sigma}_r \, \mathbf{I}$

  $\mathbf{U}_r^* \leftarrow \dfrac{\mathbf{S}_r}{\|\mathbf{S}_r\|}$

  **if** *reusePrevious AND hasConverged* **then**

    $\mathbf{A}_0 \leftarrow \mathbf{R}^T \mathbf{A} \mathbf{R}$

  **else**

    $\hat{\mathbf{A}}_0 \leftarrow \hat{\mathbf{U}}_0$

  **end**

  *hasConverged* $\leftarrow$ False

  $\hat{\mathbf{A}}_r^* \leftarrow \underset{\hat{\mathbf{A}} \in \mathbb{R}^5}{\operatorname{argmin}} \|\mathbf{F}(\hat{\mathbf{A}}_r, \hat{\mathbf{U}}_r^*)\|$ given $\hat{\mathbf{A}}_0$ `// see` (3.33)-(3.37)

  **if** $\|\mathbf{F}(\hat{\mathbf{A}}_r^*, \hat{\mathbf{U}}_r^*)\| < f_{\text{tol}}$ **then**

    *hasConverged* $\leftarrow$ True

    $\mathbf{A} \leftarrow \mathbf{R} \mathbf{A}_r^* \mathbf{R}^T$

    $r_\alpha \leftarrow \frac{\mathbf{A}_{22}}{\mathbf{A}_{33}}$

    $y_\alpha \leftarrow \sqrt{3/2} \|\mathbf{S}_H(\mathbf{A})\|$

    $\mathbf{o} \leftarrow \mathbf{o} + (\alpha, r_\alpha, y_\alpha)$ `// extend the sequence o`

  **end**

**end**

**return o**

**Algorithm 3:** VEF algorithm for calculating material state evolution under the imposed deviatoric stress mode $\mathbf{U}^*$

**Input**: stress mode: $\mathbf{U}^*$, maximal von Mises strain: $\varepsilon_{\max}$, increment of von Mises strain: $\Delta\varepsilon$, accuracy threshold: $f_{\text{tol}}$
**Result**: sequence of triplets $(\varepsilon, \mathbf{A}, \mathbf{S}_H(\mathbf{A}))$: $\mathbf{o}$

$\boldsymbol{\varepsilon}_{\text{total}} \leftarrow 0$
$\hat{\mathbf{A}}_0 \leftarrow \hat{\mathbf{U}}^*$
$\mathbf{o} \leftarrow \emptyset$
**while** $\sqrt{2/3}\|\boldsymbol{\varepsilon}_{\text{total}}\| < \varepsilon_{\max}$ **do**
  $\hat{\mathbf{A}}^* \leftarrow \underset{\hat{\mathbf{A}} \in \mathbb{R}^5}{\operatorname{argmin}} \|\mathbf{F}(\hat{\mathbf{A}}, \hat{\mathbf{U}}^*)\|$ given $\hat{\mathbf{A}}_0$ `// see (3.33)-(3.37)`
  **if** $\|\mathbf{F}(\hat{\mathbf{A}}^*, \hat{\mathbf{U}}^*)\| < f_{\text{tol}}$ **then**
    $\Delta\boldsymbol{\varepsilon} \leftarrow \Delta\varepsilon \mathbf{A}^*$
    $\mathbf{o} \leftarrow \mathbf{o} + (\varepsilon, \mathbf{A}^*, \mathbf{S}_H(\mathbf{A}^*))$ `// extend the sequence o`
    Update CP state variables by applying $\Delta\boldsymbol{\varepsilon}$
    $\boldsymbol{\varepsilon}_{\text{total}} \leftarrow \boldsymbol{\varepsilon}_{\text{total}} + \Delta\boldsymbol{\varepsilon}$
  **else**
    **return o**
  **end**
**end**

The slip systems are defined by the family of symmetrically equivalent slip planes and associated family of slip directions. For instance, in fcc materials there are 12 slip systems given by $\{011\}\langle 100\rangle$. The definition of a slip system $(s)$ includes the unit vector $\mathbf{m}^{(s)}$, which is normal to a slip plane that allows shear deformation realized by a dislocation glide. The kinematical equation that relates $\mathbf{d}$ with the slip rates $\dot{\gamma}^{(s)}$ of all active slip systems reads

$$\mathbf{d} = \sum_{s=1}^{N} \mathbf{M}^{(s)} \dot{\gamma}^{(s)} \tag{3.41}$$

where the Schmid tensor $\mathbf{M}^{(s)}$ relates the normal to the slip plane with the normalized shear direction $\mathbf{b}^{(s)}$ in which the slip occurs:

$$\mathbf{M}^{(s)} = \frac{1}{2}\left(\mathbf{b}^{(s)} \otimes \mathbf{m}^{(s)} + \mathbf{m}^{(s)} \otimes \mathbf{b}^{(s)}\right) \tag{3.42}$$

The slip systems that satisfy $\dot{\gamma}^{(s)} \neq 0$ are referred to as the active slip systems. The unknown slip rates can be determined under the energetic assumption, which postulates that minimal plastic work is dissipated per unit time:

$$\dot{W} = \sum_{s=1}^{N} \tau_c^{(s)} |\dot{\gamma}^{(s)}| \rightarrow \min \tag{3.43}$$

where $\tau_c^s$ is the critical resolved shear stress (CRSS) of the slip system $(s)$. Although the CRSS can in principle be expressed as a function of the accumulated shear in the slip system, in the present considerations the hardening of the slip systems is neglected. Furthermore, all the slip systems are supposed to have identical CRSS. The generality of the presented approach is not undermined by these assumptions, since they can be easily lifted. Moreover, one may argue that for certain classes of materials, such as fcc, the texture evolution and induced plastic anisotropy remain practically insensitive to the microscopic hardening model. This of course does not generally hold for all types of materials. On the other hand, even a very simple microscopic hardening law may become beneficial in handling complex hardening phenomena (e.g. differential hardening effect), as it was recently demonstrated by Eyckens et al. (2015).

Unfortunately, many combinations of slip systems may possibly satisfy (3.41) and (3.43) simultaneously, which is called Taylor ambiguity. To determine which slip systems are actually activated, an additional criterion is generally needed. The interested reader is referred to a recent review by Mánik and Holmedal (2014) for a comprehensive study of various means to solve the Taylor ambiguity. One of possible solutions to the issue is to consider a cluster of grains that impose constraints on each other (Van Houtte et al. 2005).

Once the slip rates are known, the deviatoric stress tensor $\mathbf{s}$ can be calculated, either directly by using the Bishop-Hill theory (Bishop and Hill 1951b), or by using the minimization method (3.43) and considering it as the work-conjugate to the imposed strain rate:

$$\dot{W} = \mathbf{s} : \mathbf{d} \tag{3.44}$$

It also follows that texture evolution can be then predicted as well. The lattice spin $\mathbf{w}^L$, which causes reorientation of the crystal lattice and in turn texture evolution, can be found from the slip rates in each grain:

$$\mathbf{w} = \mathbf{w}^L + \sum_{s=1}^{N} \mathbf{M}_A^{(s)} \dot{\gamma}^s \tag{3.45}$$

given the anti-symmetric part of the velocity gradient tensor (3.40). $\mathbf{M}_A^{(s)}$ is the anti-symmetric complement to the Schmid tensor:

$$\mathbf{M}_A^{(s)} = \mathbf{b}^{(s)} \otimes \mathbf{m}^{(s)} - \mathbf{M}^{(s)} = \frac{1}{2}\left(\mathbf{b}^{(s)} \otimes \mathbf{m}^{(s)} - \mathbf{m}^{(s)} \otimes \mathbf{b}^{(s)}\right) \tag{3.46}$$

As we can see, this way the evolution of the microscopic state variables $\mathbf{z}$ is accounted for.

The ALAMEL homogenization scheme postulates that clusters of two grains have to be treated jointly. The two grains are assumed to be neighbours, i.e. they are separated by a grain boundary. The boundary is characterized by its orientation, which at the same time defines a local orthogonal reference frame. By convention, the 3rd axis of the grain boundary reference frame is parallel to the grain boundary normal. The scheme allows relaxations of the macroscopic velocity gradient with respect to simple shear along the boundary between the grains:

$$\mathbf{l}^{(grain_1)} = \mathbf{L} + \sum_{j=1}^{2} \mathbf{K}_{RLX}^{(j)} \dot{\gamma}_{RLX}^{(j)} \tag{3.47}$$

$$\mathbf{l}^{(grain_2)} = \mathbf{L} - \sum_{j=1}^{2} \mathbf{K}_{RLX}^{(j)} \dot{\gamma}_{RLX}^{(j)} \tag{3.48}$$

As can be seen, the relaxations in both grains are equal with respect to the magnitude, but oriented in opposite directions. The relaxation slip rates $\dot{\gamma}_{RLX}^{(j)}$ conceptually operate on pseudo slip systems which are shared by the two grains, whereas the slip rates and local spin rates of the clustered grains are different. The relaxation matrices in the grain boundary reference frame are defined as:

$$\mathbf{K}_{RLX}^{(1)} = \begin{bmatrix} 0 & 0 & 1 \\ 0 & 0 & 0 \\ 0 & 0 & 0 \end{bmatrix} \quad \mathbf{K}_{RLX}^{(2)} = \begin{bmatrix} 0 & 0 & 0 \\ 0 & 0 & 1 \\ 0 & 0 & 0 \end{bmatrix} \tag{3.49}$$

Assuming that the two grains have to simultaneously satisfy the energetic assumption, Eq. (3.43) has to be reformulated as:

$$\dot{W} = \sum_{i=1}^{2} \sum_{s=1}^{N} \left\{ \tau_c^{(i,s)} |\dot{\gamma}^{(i,s)}| \right\} + \sum_{j}^{2} \tau_r^{(j)} \dot{\gamma}_{RLX}^{(j)} \rightarrow \min \tag{3.50}$$

where the index $i$ refers to the grains in the pair. Van Houtte et al. (2005) suggest to neglect the pseudo-slip term, although some artificial resistance of the pseudo-slip systems can, in principle, be introduced by letting $\tau_r^{(j)} \neq 0$.

The homogenized stress in the polycrystal is considered as the volume average of contributions from all the grains in the polycrystalline. Let $V_i$ denote the volume of the $i$th grain. Provided that the stress tensor in the individual crystals is expressed in the sample reference frame, the homogenized deviatoric part of Cauchy stress is calculated as follows:

$$\boldsymbol{S}_H = \left( \sum_{i=1}^{n} V_i \right)^{-1} \sum_{i=1}^{n} V_i \boldsymbol{s}_i \tag{3.51}$$

It is worth mentioning in this context that the virtual experiments used in calibrating macroscopic yield loci are often stress driven (or at least some idealized stress state is more opportune as the boundary condition), whereas the ALAMEL model requires macroscopic velocity gradient or strain rate as input. In the previous paragraphs we presented a method how to numerically convert a strain rate driven model so the stress is imposed as the input. It is clear from (3.43) to (3.44) that the stress state of individual grains in the polycrystalline may deviate from the imposed stress, yet the homogenized stress over the aggregate can still satisfy

$$\|\mathbf{S}_H - \mathbf{S}\| < \delta \tag{3.52}$$

where $\delta$ is a sufficiently small number. A stronger requirement (i.e. $\|\mathbf{S}_H - \mathbf{S}\| = 0$) might be difficult to satisfy given the fact that only a finite number of crystals is used in the discretized texture.

It can be argued that (3.52) introduces long range interactions in the model, since certain conditions have to be met over the whole polycrystal. Yet it needs to be emphasized that no iso-stress assumption is made concerning the aggregate.

**Hierarchical multi-scale model of cup drawing test** The presented modelling framework allows one to simulate the deformation of large parts, comparable in size to body car components. In this example we use it to simulate one of the most convenient mechanical tests assessing anisotropy of the sheet metal: the cup drawing process that forms cylindrical cups from circular blanks. We shall also investigate how the results of the adaptive multi-scale model compare to more conventional simulation of the same process and to experimental data.

Briefly, let us consider the following test cases:

HMS-BBC2008: adaptive hierarchical multi-scale model is used. The plastic anisotropy is modelled by adaptively recalculated BBC2008p16 yield criterion. The crystal plasticity model predicts texture evolution and calculates data needed for recalibration of the BBC2008p16, as it was described in the previous sections.

CP-BBC2008: hierarchical multi-scale model is used, but the plastic anisotropy is kept constant throughout the simulation. This means the crystal plasticity model uses just the initial texture data at the pre-processing stage, and thus it provides only the initial yield surface data for identifying the BBC2008p16.

Mech-BBC2008: The BBC2008p16 is conventionally calibrated by mechanical testing data.

In the case study presented below we use Al alloy AA6016 metallic sheet (1 mm nominal thickness). This material is a precipitation hardening alloy, containing aluminum, magnesium and silicon as major components. The sheet has been delivered in the T4 status (solution heat treated and naturally aged). One of the major applications of this material is in the automotive industry. Admittedly, the AA6016-T4 has a rather mild anisotropy, which furthermore does not change much

during mechanical tests. Modern sheet metal materials are designed (on very purpose!) to retain their anisotropic properties approximately constant during processing. Keeping that in mind, we decided to choose a material that is realistic and actually used in industrial practice. If we selected a material that is more suitable for illustrative purposes, such as commercial purity aluminum, it would be less relevant from the application point of view.

The most conventional way of calibrating the BBC2008 yield criterion is to conduct a series of mechanical experiments. The characterization methods needed for calibrating the BBC2008 to mechanical data include uniaxial tensile tests and biaxial tension.[3] In order to determine the uniaxial mechanical parameters, tensile tests were performed on specimens cut at 0°, 15°, 30°, 45°, 60°, 75°, 90° from the rolling direction. The experiments were carried out using a Zwick-Roell 150kN universal tensile testing machine equipped with an extensometer with 20 mm gauge-length. The tensile tests have also provided the values of the conventional yield stress $y = R_{p0.2}$ and the Lankford coefficients ($r$-values), see Fig. 3.4a, b. The measured $r$-values reflect the plastic anisotropy at the beginning of yield. The mechanical response of the sheet in biaxial tension stress state was studied by means of two experimental setups: hydraulic bulging and thickness compression tests. The hydraulic bulging experiments allowed determining the balanced biaxial yield stress according to the methodology described by Lazarescu et al. (2011), while the thickness compression tests were performed to determine the biaxial coefficient of plastic anisotropy (Barlat et al. 2003a). The balanced biaxial yield stress was found $y_{bx} = 160.1\,\text{MPa}$, while the measurement of the biaxial coefficient of plastic anisotropy resulted in $r_{bx} = 1.037$ (cf. Fig. 3.4c).

While the conventional calibration of the BBC2208 requires fairly extensive experimental work, the virtual calibration is much more straightforward. The multi-scale model presented in the previous section requires texture data as the main microstructural input. A single experiment is needed and it consumes approximately 1 of the material. As presented in Gawad et al. (2015), X-ray diffraction technique provided the through-thickness texture and the mid-plane texture at the depth of 50 % of the sheet. The $\phi_2 = 45°$ sections of the measured ODF along with schematically depicted measurement positions are shown in Fig. 3.3.

The figure also shows the texture index (TI), which gives an overall view of texture sharpness, defined as integral over entire orientation space:

$$\text{TI} = \int f^2(g)dg \tag{3.53}$$

where $f(g)$ is the ODF. As can be seen, the sheet features a much sharper texture at the mid-plane than over the complete thickness. This indicates a presence of a complex texture gradient across the thickness, yet we shall not elaborate on this

[3]The results of mechanical experiments and texture measurements used in this section are taken from Gawad et al. (2015).

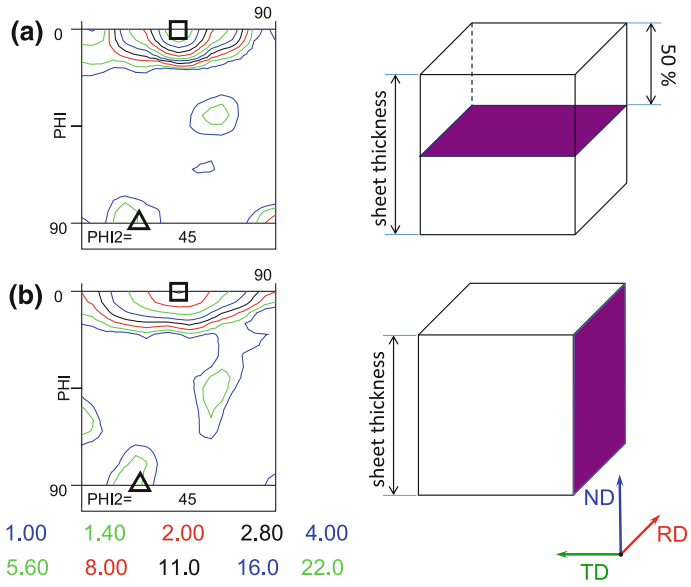


**Fig. 3.3** $\phi_2 = 45°$ ODF sections (with $\phi_1$ and $\Phi$ on horizontal and vertical axis, respectively) of the experimental textures: **a** mid-plane texture (50 % depth), TI = 4.96, and **b** through-thickness texture, TI = 2.45. Annotations indicate the *Cube component* (*square*) and the P component (*triangle*). The ODFs are expressed in identical reference frame: $x_1 =$ RD, $x_2 =$ TD and $x_3 =$ ND. Schematic sketch of the experimental texture measurement scheme is presented on the right. The *violet plane* depicts the surface exposed to the X-ray beam (Color figure online)

aspect here. Generally, the texture of this material is mostly attributed to the Cube component, i.e. the orientation given by $(\phi_1, \Phi, \phi_2) = (45°, 0°, 45°)$ in the presented ODF sections. Moreover, the spread around Cube forms a fibre towards $(45° + x, 0°, 45°)$ and $(45° - x, 0°, 45°)$. At the mid-plane however, the Cube fibre is only partial, i.e. $x < 45°$. The P texture component $(29.5°, 90°, 45°)$, which is generally attributed to the recrystallization solutionizing annealing (Engler and Hirsch 2002), can also be identified. The analyzed textures contain also some minor Goss component $\{011\}\langle 100\rangle$, which is seen in this section as a small intensity maximum at $(\phi_1, \Phi, \phi_2) = (90°, 90°, 45°)$.

The measured textures were further processed to obtain input data for the virtual experiments. Discrete ODFs, needed by the ALAMEL model, were probed from the continuous ODFs using the STAT algorithm described in Tóth and Van Houtte (1992) and implemented in the MTM-FHM software (Van Houtte 1995). Each of the initial data sets consisted of $N = 5000$ crystallographic orientations, expressed as Euler angles in Bunge (1982) convention: $\phi_1$, $\Phi$ and $\phi_2$. The number of orientations is sufficient to guarantee that the RVE represents the local macro-texture of the material.

In the next step, the crystal plasticity stress-driven virtual experiments were conducted to calculate the data points needed for identification of the BBC2008

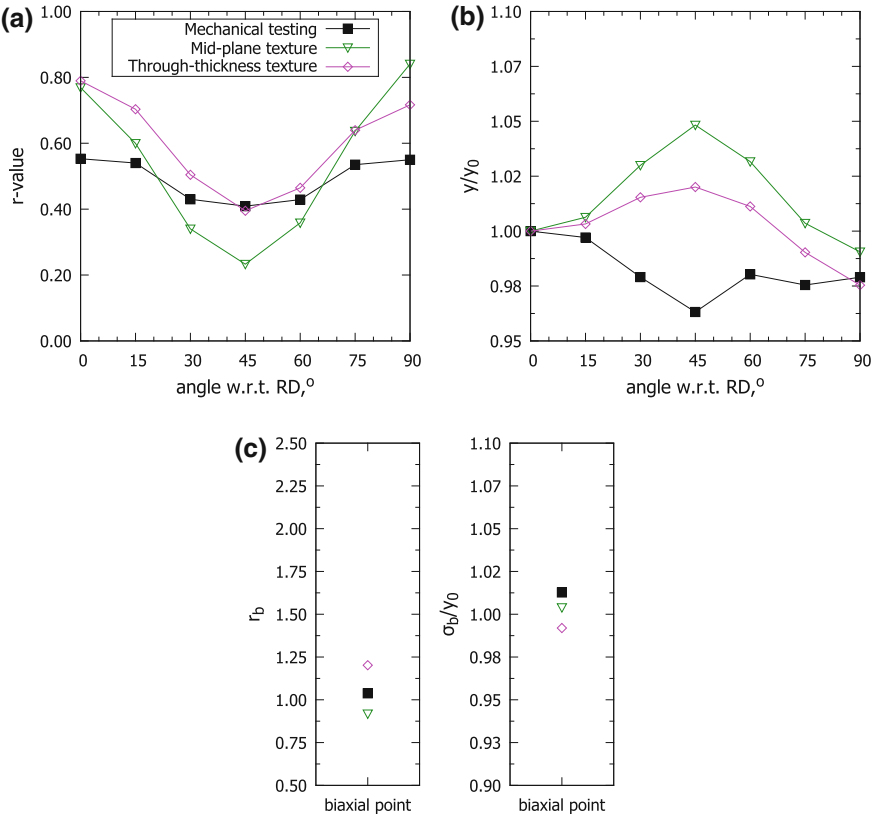


**Fig. 3.4** Initial characterization of plastic anisotropy obtained by means of the mechanical testing and virtual experiments: **a** Lankford coefficient (*r*-value), **b** uniaxial yield stress, and **c** biaxial yield stress and *r*-values. All yield stresses are scaled by the uniaxial yield stress along 0° to RD. The legend in **a** applies also to the other plots. The initial experimental textures (cf. Fig. 3.3) were used in the virtual experiments

yield criterion. Figure 3.4 presents the calculated *r*-values and the yield stresses. The directions of uniaxial loading were chosen as $\alpha = 0°, 15°, \ldots, 90°$ (cf. (3.14) and (3.15)). Since the extended identification algorithm was used (see (3.13) and more extensive description in Chap. 1), the following directions $\theta$ were used in (3.18) and (3.19) to define biaxial stress ratios: 7°, 30°, 45°, 60°, 83°, 120°, 330°. The point evaluated at $\theta = 45°$ was also used in Eqs. (3.16) and (3.17) for calculating the $r_b$ and $y_b$. Identical selection of data points was used in the simulations exploiting the CP-BBC2008 and HMS-BBC2008 model. All the weighting factors in (3.13) were set to unity, except for $w_\beta = 4$.

It can be seen from Fig. 3.4 that the uniaxial *r*-values resulting from the mechanical testing are generally consistent with the data provided by the virtual experiments. However, this is not the case if other quantities are considered. In

terms of the scaled uniaxial yield stresses, the virtual and the mechanical tests predict opposite trends: the maximum around 45° is consistently obtained in all virtual experiments, whereas the mechanical testing resulted in a minimum in this direction. As can be seen in Fig. 3.3, the variability of the experimental normalized uniaxial yield stress is bound in the range of (≈0.97, 1.0), therefore only a minor fluctuation of ≈3 % is present. Therefore, it is perfectly possible that the experimental result does not fully reflect the actual material behavior, since every measurand includes certain measurement uncertainty. At this point it remains debatable whether the crystal plasticity or the mechanical experiment provides better estimate of the actual material behavior in the considered case. Another prominent difference between the mechanical and the virtual testing is found at the equibiaxial yield point. Apart from the discrepancy in magnitude, the crystal plasticity predicts pretty much variation in the equibiaxial $r$-value, either below unity if the sharper mid-plane texture is used, or above unity for the milder through-thickness texture.

All the multi-scale simulations presented in the subsequent paragraphs use the macroscopic Swift hardening law

$$\bar{\sigma}(\varepsilon_{vM}) = K(\varepsilon_{vM} + \varepsilon_0)^n \tag{3.54}$$

where the coefficients $K = 479.7$ MPa, $n = 0.239$ and $\varepsilon_0 = 0.00096$ were determined from the average of the mechanical uniaxial tensile tests.

Concerning the cup drawing experiments, a set of cups was formed on an adapted Erichsen device. The following dimensions characterize the geometry of the tools: punch diameter: 50 mm, punch lip radius: 6 mm, die diameter: 52.82 mm and die lip radius: 3 mm, while the diameter of the blank is 90 mm. After the deep drawing, cup profiles were measured and averaged over symmetrically equivalent positions.

An Abaqus Explicit FE model was set up to reproduce the experimental cup drawing setup. Due to the symmetry of the process, it is possible to simulate one-quarter of the blank. To accelerate the computations, a mass scaling procedure was used, although quasi-static conditions were ensured. The blank was discretized using 3247 reduced integration wedge continuum shell elements (in Abaqus nomenclature: SC6R). Although only one layer of elements was used, the elements were set to include 3 integration points across the thickness. Frictional contact between the blank and the tools (punch, die and blankholder) was controlled using Coulomb law with the coefficient of friction $\mu = 0.2$, which approximately corresponds to conditions in a moderately lubricated steel-aluminum contact pair.

The HMS-BBC2008 simulations were executed on ten 12-core Westmare nodes. On average it took 5 h for an HMS-BBC2008 simulation to complete, while each of the corresponding Mech-BBC2008 and CP-BBC2008 simulations required 1 h on a single node.

The results of the simulations and experiments are summarized in Fig. 3.5. Although none of the simulations perfectly reproduces the experimental profile, it is clear that the texture-based simulations deliver superior predictions of the earing behavior. While the CP-BBC2008 and HMS-BBC2008 simulations both result in

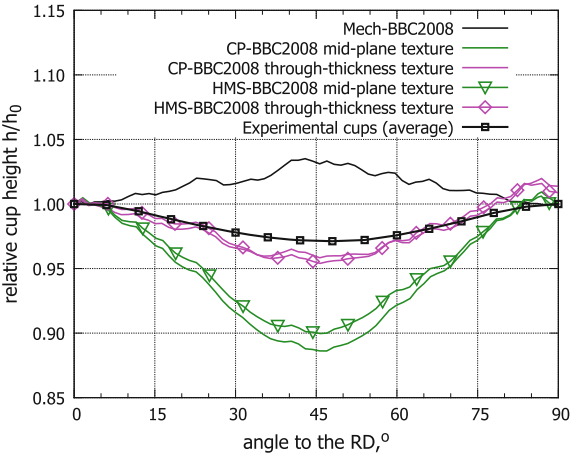


**Fig. 3.5** Comparison of experimental and predicted relative cup profiles, scaled by cup height at 0° w.r.t. RD

correctly positioned ears, the modeling that relies on mechanical testing (Mech-BBC2008) wrongly predicts the ears at 45° w.r.t. RD.

Another aspect of the cup geometry prediction is related to the intensity of texture used as the starting point. As it could be anticipated from Fig. 3.4, the sharper mid-plane texture resulted in excessively pronounced ears. With respect to the impact of anisotropy evolution on the macroscopic geometry, both CP-BBC2008 and HMS-BBC2008 provide very similar cup profile prediction. Although the results of HMS-BBC2008 are slightly closer to the experimental cup, the improvement over CP-BBC2008 is only clearly visible if the sharper mid-plane texture is used as the starting point. Furthermore, the correction due to anisotropy evolution is very minor when the relative cup profile almost agrees with the experimental cups.

This raises at least two questions: why the Mech-BBC2008 produces a considerably different cup profile, and why the anisotropy evolution accounted for in HMS-BBC2008 simulations results only in limited improvement over CP-BBC2008.

The first question can be partly answered if we recall the most significant distinction between the mechanical testing and the texture-based virtual experiments found in Fig. 3.4. The mechanical testing resulted in a minimum of uniaxial yield stresses in the direction around 45° w.r.t. RD, as opposed to the virtual tests that predict it elsewhere. This minimum may appear to be a factor associated with the position of the valleys, for the reason that they correspond to higher resistance to tension in both RD and TD.

The stress state in the flange, nevertheless, is dominantly imposed by the geometry of the process. Furthermore, it considerably differs from uniaxial tension. Depending on the radial position in the flange, it may vary from nearly pure compression along the circumferential direction (at the outer rim) to a superposition of tension along the radial direction and predominant compression along the circumference. Suppose the total strain tensor is expressed in a cylindrical coordinate

system given by the axes $(\mathbf{e}_r, \mathbf{e}_\psi, \mathbf{e}_z)$. The origin of the coordinate system is fixed and coincides with the centre of the blank, while the axes correspond to the radial direction of the blank, angular position along the circumference and the sheet normal, respectively. The ratio between the radial and tangential stress in a single material point also changes while the process advances. It may be ≈–0.1 at the beginning of the process, whereas it may reach ≈–0.8 when the material point approaches the bending zone near the die lip. The plastic flow, which is a consequence of the stress state, can be then described by the ratio

$$e = \frac{\varepsilon_{rr}}{\varepsilon_{\psi\psi}} \tag{3.55}$$

between the radial and tangential strains ($\varepsilon_{rr}$ and $\varepsilon_{\psi\psi}$, respectively). Since the strain components are in a direct relation with the yield locus through the strain rates calculated from the normality rule, the $e$-ratio depends on the yield locus shape as well. The strain evolution of the $e$-ratio was tracked in three finite elements, initially located at identical radius $r = 40$ mm along the RD, TD and 45° w.r.t. RD. Since the instantaneous stress state is used, different points on the yield locus are probed. The strain range was chosen to ensure that the considered material points remain sufficiently far from the die lip, and at the same time $\sigma_{zz} \approx 0$.

Figure 3.6 shows the $e$-ratio calculated for a subset of the considered cup drawing simulations. For the sake of clarity, the figure includes just the results of the Mech-BBC2008, and two CP-BBC2008 and HMS-BBC2008 that are both started from the through-thickness texture. The most pronounced difference between the two crystal plasticity based simulations and the one based on the mechanical testing data is visible at the RD and TD locations. This particularly holds at the onset of the plastic deformation, when the stress state in the given coordinate system remains nearly identical in all the cases. Thus, the divergence in the material flow is most likely attributed to the shape of the explored yield locus regions. It appears that the relatively limited deviation from the uniaxial tension state results in probing the yield surface in regions of remarkably different curvature.

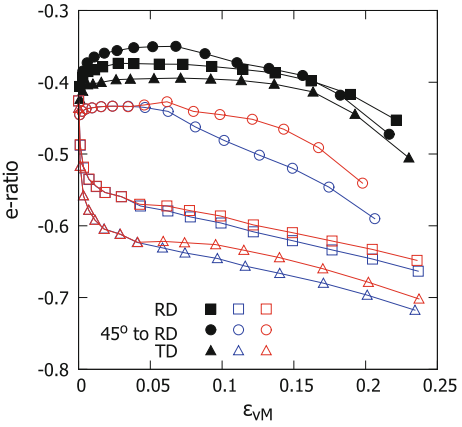


**Fig. 3.6** Evolution of $e$-ratio as a function of equivalent von Mises plastic strain in the cup drawing simulations at the selected points in the flange: RD, 45° to RD and TD: Mech-BBC2008 (*closed black symbols*), CP-BBC2008 (*open blue symbols*) and HMS-BBC2008 (*open red symbols*), respectively (Color figure online)

If the yield locus model is calibrated primarily to the uniaxial tension data, as it is the case if the mechanical testing data are used, the regions of the yield locus that are actually reached in the cup drawing simulation are relatively distant from the measurement points. The yield loci derived from the virtual experiments, by contrast, are constructed by exploiting data points of various stress ratios. One may hence expect these yield loci to be more reliable, since the stress states more relevant to the cup drawing process are sampled.

Figure 3.6a also offers a hint why and the anisotropy evolution has only a minor effect on the cup profile. It is clearly visible that the strain history of the $e$-ratio coincides in the CP-BBC2008 and HMS-BBC2008 simulations only until the very first update of the yield locus model. Nonetheless, the subsequent change in the flow direction appears minor.

To explain this, let us examine how the fine-scale material state evolves and to what extent it impacts the anisotropy. Figure 3.7 presents an example of simulated cups with a superimposed field showing the count of anisotropy updates. As can be expected from Eq. (3.1), the field variable is tightly correlated with the magnitude of the plastic strain. Thus, the regions of the highest plastic strain have been updated multiple times and possibly the texture has been altered to a large extent. This is indeed the case, as seen in Fig. 3.8 showing the texture index derived from the micro-scale state and superimposed on the deformed finite element mesh. In both HMS-BBC2008 simulations we can observe a complex texture pattern that develops in the formed cup. It is remarkable that the overall texture sharpness rapidly decreases if the stronger mid-plane texture is used as the starting point, whereas the milder through-thickness texture in certain zones of the cup slightly intensifies.

It is difficult to examine evolution histories in all individual integration points. Let us then explore more in detail how the micro-scale material state and anisotropy evolve in a selected integration point located approximately 3 away from the cup rim at the RD. Figure 3.9 presents the final deformation textures that the HMS-BBC2008 model predicted in that location. In principle, texture evolution may destroy the original orthorhombic symmetry (as it was used in Fig. 3.3), thus no symmetries are imposed in the figure. The ODFs are plotted in the coordinate system coinciding with the material co-rotational reference frame. A visual inspection reveals a substantial change from the initial ODFs shown in Fig. 3.3. Even though the Cube component remains the most intense texture feature, a new texture component is regularly found. The Cu (Copper) component of varying intensity emerges in both analyzed textures, most remarkably in the evolved mid-plane texture, where it appears almost equally pronounced as the Cube component. Interestingly, the Goss component remains at similar intensity level as it used to be in the initial textures. At this point we may conclude the texture has undergone a considerable evolution during the deformation.

One might expect that not only the texture but also the anisotropic properties shall be far from the initial ones. The local anisotropy indeed evolves, as shown in yield loci shown in Fig. 3.10. The initial yield locus and the one that evolved at the considered location are substantially different, yet the largest changes are seen in the

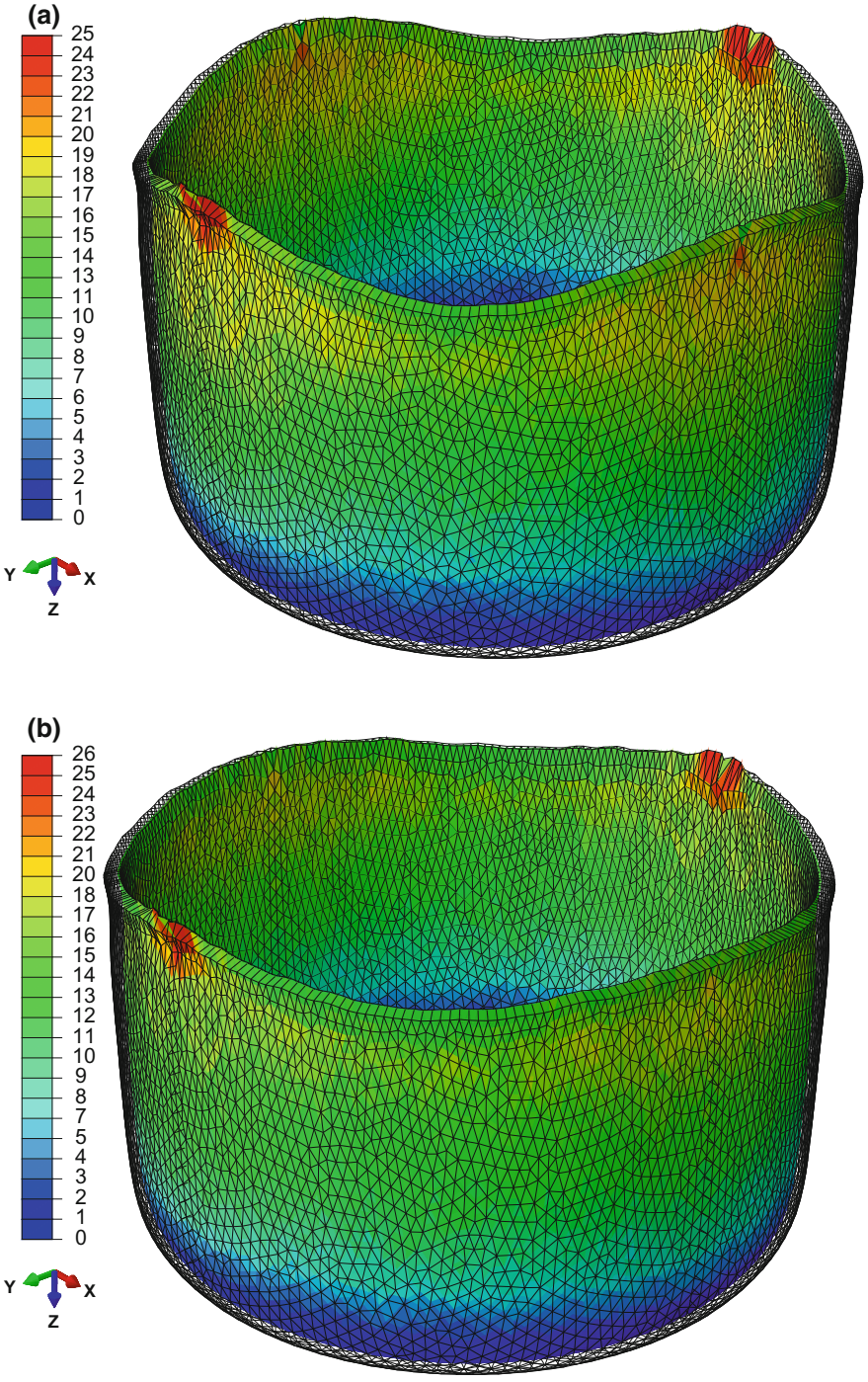


**Fig. 3.7** Number of updates of texture and anisotropy in the HMS-BBC2008 simulations, presented as a field projected on the final cups (symmetries on the XZ and YZ planes are superimposed). **a** Mid-plane texture, and **b** through-thickness texture are used as the initial textures

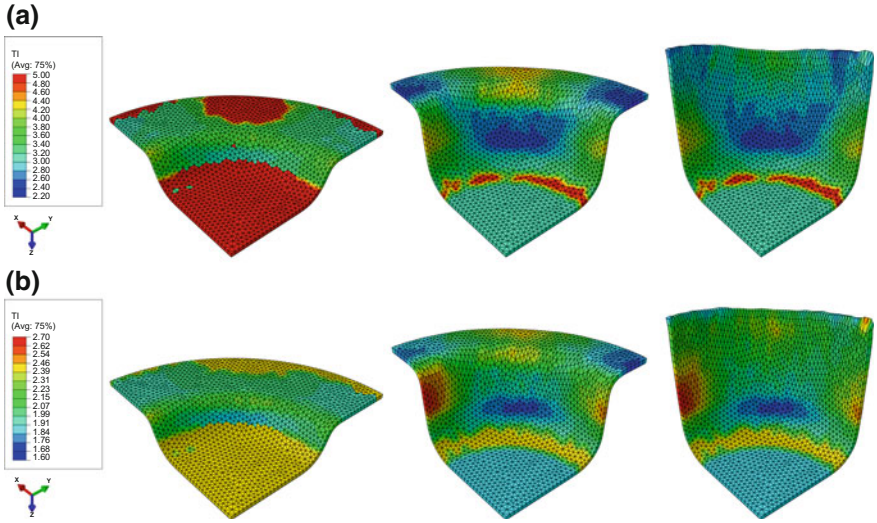


**Fig. 3.8** Texture index at successive deformation stages superimposed on the deformed FE mesh in simulations started from **a** mid-plane texture (initial TI = 4.96), and **b** through-thickness texture (initial TI = 2.45), respectively

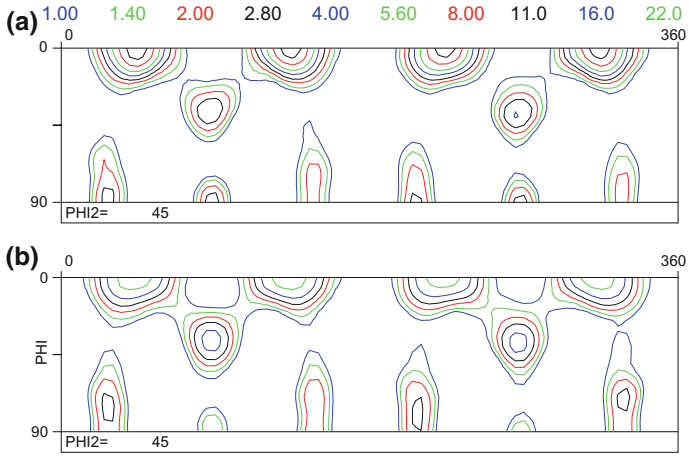


**Fig. 3.9** $\phi_2 = 45°$ ODF sections (with $\phi_1$ and $\Phi$ on the horizontal and the vertical axis, respectively) of the final texture textures that evolved from: **a** mid-plane texture (TI = 3.05), and **b** through-thickness texture (TI = 2.26) in the analysed position. Both sections are presented in the identical corotational reference frame, which initially was given by $x_1$ = RD, $x_2$ = TD and $x_3$ is the normal to the sheet

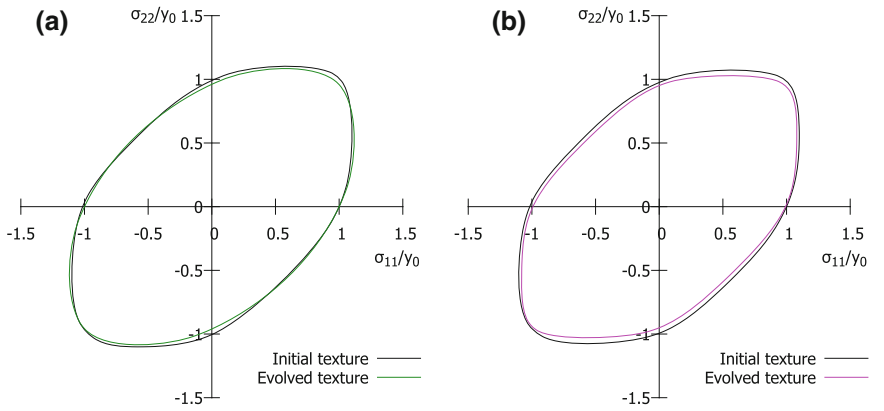


**Fig. 3.10** Comparison of the initial and final yield loci obtained in the HMS-BBC2008 simulations that used **a** mid-plane texture, and **b** through-thickness texture, respectively

yield locus regions that are not active in the cup drawing process. This basically suggests a texture-induced cross-effect, which partly explains limited impact of texture evolution on the macroscopic geometry of the cup. Figure 3.11 summarises the uniaxial characteristics of plastic anisotropy that were obtained for the final deformation textures in the same geometrical location. With regard to the effects of texture evolution on the plastic behavior under uniaxial loading, the *r*-values are moderately affected. Much more complex evolution is observed when the uniaxial yield stresses are considered. Those not only tend to decrease, but the monotonicity is influenced as well: the maximum at direction 45° in the initial material clearly diminishes for the mid-plane texture.

Let us finally check a key aspect in the adaptive hierarchical modelling, namely the ability of the macroscopic yield locus to provide a good approximation of virtual experiments. From Fig. 3.11, which also shows how the BBC2008p16 predicts uniaxial material response, it is clear that the BBC2008 reproduces the virtual experiments remarkably well and is generally capable of following the changes in anisotropy that occur during the deformation.

### *3.3.4 Other Concepts in Multi-scale Modelling of Plastic Anisotropy*

It is hardly possible to give a complete and comprehensive overview of all the concepts that have been investigated in the field of multi-scale modelling of plastic anisotropy. In this short section we want to mention a few interesting approaches that explore areas beyond the scope presented in the previous sections.

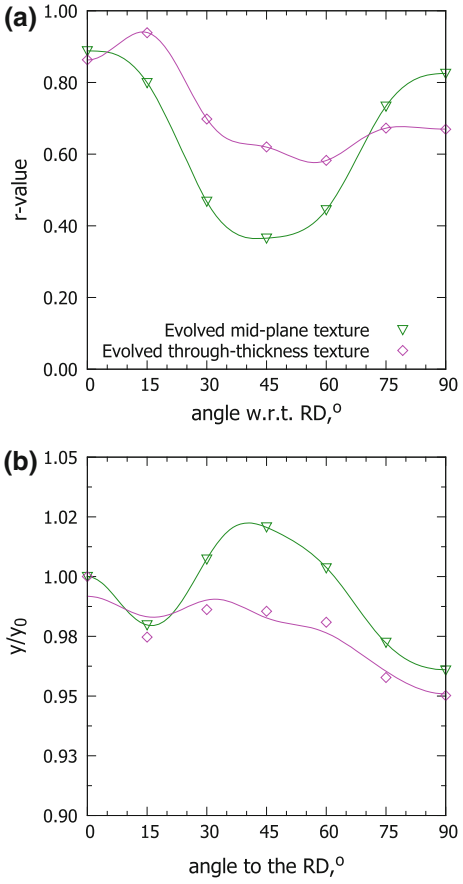


**Fig. 3.11** **a** *r*-values, and **b** scaled uniaxial yield stresses calculated from evolved textures in the simulated fully formed cups: ALAMEL-based virtual experiments (*symbols*), BBC2008 local yield locus calibrated to the virtual experiments (*lines*). The legend in **a** applies to both plots

One of such concepts is to develop a macroscopic constitutive model that would allow deriving the current plastic anisotropy directly from instantaneous crystallographic texture or from constituents of crystal plasticity frameworks, see e.g. Arminjon and Bacroix (1991), Kowalczyk and Gambin (2004), Tsotsova and Böhlke (2009). Several attempts to derive macroscopic yield loci directly from texture data (i.e. without using any CP framework) have been reported in the literature. For instance, one can try to associate various texture components with their contributions to the global mechanical behaviour. This way an analytical yield locus can be constructed, as it has been tested in Darrieulat and Montheillet (2003), Darrieulat and Piot (1996). The authors investigated how parameters of quadratic Hill yield criterion can be analytically derived for the most common rolling textures. In the further step, a rule of mixture was followed to construct the Hill criterion that combines contributions from individual texture components. However, this method silently ignores the contribution from minor texture components, which may be more than subtle if interactions between the contributing terms play a role.

As the CP appears to set more reliable and robust means to recover mechanical data from the microstructure, computational performance of virtual experiments becomes crucial. This point is recognized for instance in the Reduced Texture Methodology (RTM) proposed in Rousselier and Leclercq (2006), Rousselier et al. (2009). The RTM aims neither at a complete representation of the real material texture, nor at an accurate modeling of its evolution, but it focuses on accelerating the virtual experiments. This can be achieved by simplifying the crystal plasticity model (e.g. Rousselier and Leclercq 2006). At the expense of dropping certain physical grounds, some computational gains can be reached. For example, a concept of individual crystals with smooth yield surfaces was investigated in Arminjon and Bacroix (1991), Gambin and Barlat (1997), Gambin (1992), Zamiri et al. (2007), Zamiri and Pourboghrat (2010), among others. In this formulation one yield function is used at the crystal level to calculate the crystal spin and the shear rates at the same time. Since these yield surfaces have rounded corners, as opposed to crystal yield surfaces calculated by resolving slip systems, the problem of non-uniqueness in the choice of active slip systems vanishes.

Since simplifications in the fundamental parts of the crystal plasticity may possibly impair predictive capabilities of the model, another way of accelerating virtual experiments (or to put it broader: enhancing computational performance of RVEs) is to reduce the number of crystal orientations per integration point of the macroscopic FE mesh. This is built on an observation that in many cases crystallographic textures can be approximated by a rather small number of texture components. Several attempts have been proposed to limit the number of orientations that have to be processed by the crystal plasticity while retaining a good prediction of both texture and anisotropy evolution, see e.g. Béringhier et al. (2007), Böhlke et al. (2005), Delannay et al. (2005), Knezevic and Landry (2015), Logé and Chastel (2006), Raabe et al. (2004), Raabe and Roters (2004), Roters (2005), Zhao et al. (2004).

**Acknowledgments** The authors would like to extend sincere gratitude to the co-authors of their previous papers on hierarchical multi-scale modelling. In particular, the authors gratefully acknowledge fruitful and formulating discussions with Profs. D. Roose and D. Banabic, and Dr. P. Eyckens. We also gratefully acknowledge financial support from the Knowledge Platform M2Form, funded by the Industrial Research Fund of KU Leuven.

## References

Al-Harbi HF, Knezevic M, Kalidindi SR (2010) Spectral approaches for the fast computation of yield surfaces and first-order plastic property closures for polycrystalline materials with cubic-triclinic textures. Comput Mater Contin 15(2):153–172

Alharbi HF, Kalidindi SR (2015) Crystal plasticity finite element simulations using a database of discrete Fourier transforms. Int J Plast 66:71–84

An Y, Vegter H, Carless L, Lambriks M (2011) A novel yield locus description by combining the Taylor and the relaxed Taylor theory for sheet steels. Int J Plast 27(11):758–1780

Aretz H, Barlat F (2012) Unconditionally convex yield functions for sheet metal forming based on linear stress deviator transformation. Key Eng Mater 504–506:667–672. ISBN:978-3-03785-366-5

Aretz H, Barlat F (2013) New convex yield functions for orthotropic metal plasticity. Int J Non-linear Mech 51:97–111

Arminjon M, Bacroix B (1991) On plastic potentials for anisotropic metals and their derivation from the texture function. Acta Mech 88(3–4):219–243

Arsenlis A, Barton NR, Becker R, Rudd RE (2006) Generalized in situ adaptive tabulation for constitutive model evaluation in plasticity. Comput Methods Appl Mech Eng 196(1–3):1–13

Arul Kumar M, Mahesh S, Parameswaran V (2011) A 'stack' model of rate-independent polycrystals. Int J Plast 27(6):962–981

Asaro RJ (1983a) Crystal plasticity. J Appl Mech 50(4b):921

Asaro RJ (1983b) Advances in applied mechanics, vol 23. Elsevier. ISBN:9780120020232

Asaro RJ, Needleman A (1985) Overview no. 42 texture development and strain hardening in rate dependent polycrystals. Acta Metall 33:923–963

Asaro RJ, Rice JR (1977) Strain localization in ductile single crystals. J Mech Phys Solids 25(5):309–338

Banabic D, Comsa DS, Balan T (2000) A new yield criterion for orthotropic sheet metals under plane stress conditions. In The 7th Conference TPR2000, Cluj Napoca, pp 217–224

Banabic D, Kuwabara T, Balan T, Comsa DS, Julean D (2003) Non-quadratic yield criterion for orthotropic sheet metals under plane-stress conditions. Int J Mech Sci 45(5):797–811

Banabic D, Aretz H, Comsa DS, Paraianu L (2005) An improved analytical description of orthotropy in metallic sheets. Int J Plast 21(3):493–512

Banabic D, Barlat F, Cazacu O, Kuwabara T (2010) Advances in anisotropy and formability. Int J Mater Forming 3(3):165–189

Barlat F, Becker RC, Hayashida Y, Maeda Y, Yanagawa M, Chung K, Brem JC, Lege DJ, Matsui K, Murtha SJ, Hattori S (1997a) Yielding description for solution strengthened aluminum alloys. Int J Plast 13(4):385–401

Barlat F, Maeda Y, Chung K, Yanagawa M, Brem JC, Hayashida Y, Lege DJ, Matsui K, Murtha SJ, Hattori S, Becker RC, Makosey S (1997b) Yield function development for aluminum alloy sheets. J Mech Phys Solids 45(11–12):1727–1763

Barlat F, Brem JC, Yoon JW, Chung K, Dick RE, Lege DJ, Pourboghrat F, Choi S-H, Chu E (2003a) Plane stress yield function for aluminum alloy sheets—part I: theory. Int J Plast 19(9):1297–1319

Barlat F, Ferreira Duarte JM, Gracio JJ, Lopes AB, Rauch EF (2003b) Plastic flow for non-monotonic loading conditions of an aluminum alloy sheet sample. Int J Plast 19(8):1215–1244

Barlat F, Aretz H, Yoon JW, Karabin ME, Brem JC, Dick RE (2005) Linear transformation-based anisotropic yield functions. Int J Plast 21(5):1009–1039

Barlat F, Yoon JW, Cazacu O (2007) On linear transformations of stress tensors for the description of plastic anisotropy. Int J Plast 23:876–896

Barlat F, Lege DJ, Brem JC (1991) A six-component yield function for anisotropic materials. Int J Plast 7(7):693–712

Barton NR, Knap J, Arsenlis A, Becker R, Hornung RD, Jefferson DR (2008) Embedded polycrystal plasticity and adaptive sampling. Int J Plast 24(2):242–266

Beaudoin AJ, Mathur KK, Dawson PR, Johnson GC (1993) Three-dimensional deformation process simulation with explicit use of polycrystal plasticity models. Int J Plast 9(7):833–860

Beausir B, Suwas S, Tóth LS, Neale KW, Fundenberger J-J (2008) Analysis of texture evolution in magnesium during equal channel angular extrusion. Acta Mater 56(2):200–214

Béringhier M, Delannay L, Chastel Y, Logé R (2007) Using Lagrangian particles to efficiently describe microstructure evolution in metal forming—application to texture-induced mechanical anisotropy. Model Simul Mater Sci Eng 15(3):191–204

Bishop JFW, Hill R (1951a) A theory of the plastic distortion of a polycrystalline aggregate under combined stresses. Philos Mag 42:414–427

Bishop JFW, Hill R (1951b) A theoretical derivation of the plastic properties of a face-centred metal. Philos Mag 42:1298–1307
Böhlke T, Risy G, Bertram A (2005) A texture component model for anisotropic polycrystal plasticity. Comp Mat Sci 32(3–4):284–293
Bunge HJ (1982) Texture analysis in materials science. Butterworth, London
Bunge HJ, Esling C (1984) Texture development by plastic deformation. Mat Metall 18(3):191–195
Cazacu O, Barlat F (2004) A criterion for description of anisotropy and yield differential effects in pressure-insensitive metals. Int J Plast 20(11):2027–2045
Cazacu O, Plunkett B, Barlat F (2006) Orthotropic yield criterion for hexagonal closed packed metals. Int J Plast 22(7):1171–1194
Coenen EWC, Kouznetsova VG, Bosco E, Geers MGD (2012a) A multi-scale approach to bridge microscale damage and macroscale failure: a nested computational homogenization-localization framework. Int J Fract 178(1–2):157–178
Coenen EWC, Kouznetsova VG, Geers MGD (2012b) Multi-scale continuous–discontinuous framework for computational–homogenization–localization. J Mech Phys Solids 60(8):1486–1507
Comsa D, Banabic D (2008) Plane-stress yield criterion for highly-anisotropic sheet metals. In: Numisheet 2008. Interlaken pages, pp 43–48
Conn AR, Gould NIM, ToInt PL (2000) Trust-region methods. SIAM Society for Industrial and Applied Mathematics
Crumbach M, Pomana G, Wagner P, Gottstein G (2001) Taylor type deformation texture model considering grain interaction and material properties. part I—fundamentals. In: Gottstein G, Molodov DA (eds) Proceedings of the 1st joint international conference on recrystallisation and grain growth. Springer, Berlin, pp 1053–1060
Darrieulat M, Montheillet F (2003) A texture based continuum approach for predicting the plastic behaviour of rolled sheet. Int J Plast 19(4):517–546
Darrieulat M, Piot D (1996) A method of generating analytical yield surfaces of crystalline materials. Int J Plast 12(5):575–610
Dawson PR, Boyce DE, Hale R, Durkot JP (2005) An isoparametric piecewise representation of the anisotropic strength of polycrystalline solids. Int J Plast 21(2):251–283
Delaire F, Raphanel JL, Rey C (2000) Plastic heterogeneities of a copper multicrystal deformed in uniaxial tension: experimental study and finite element simulations. Acta Mater 48(5):1075–1087
Delannay L (2002) Prediction of intergranular strains in cubic metals using a multisite elastic-plastic model. Acta Mater 50(20):5127–5138
Delannay L, Kalidindi SR, Van Houtte P (2002) Quantitative prediction of textures in aluminium cold rolled to moderate strains. Mat Sci Eng: A 336(1–2):233–244
Delannay L, Béringhier M, Chastel Y, Logé RE (2005) Simulation of cup-drawing based on crystal plasticity applied to reduced grain samplings. Mat Sci Forum 495–497:1639–1644
Delannay L, Melchior MA, Signorelli JW, Remacle J-F, Kuwabara T (2009) Influence of grain shape on the planar anisotropy of rolled steel sheets—evaluation of three models. Comput Mater Sci 45(3):739–743
Duchêne L, Godinas A, Cescotto S, Habraken AM (2002) Texture evolution during deep-drawing processes. J Mat Proc Tech 125–126:110–118
Ebeling T, Hartig Ch, Laser T, Bormann R (2009) Material law parameter determination of magnesium alloys. Mater Sci Eng A 527(1–2):272–280
Eisenlohr P, Tjahjanto DD, Hochrainer T, Roters F, Raabe D (2009a) Texture prediction from a novel grain cluster-based homogenization scheme. Int J Mater Form 2(S1):523–526
Eisenlohr P, Tjahjanto DD, Hochrainer T, Roters F, Raabe D (2009b) Comparison of texture evolution in fcc metals predicted by various grain cluster homogenization schemes. Int J Mater Res 100(4):500–509
Eisenlohr P, Diehl M, Lebensohn RA, Roters F (2013) A spectral method solution to crystal elasto-viscoplasticity at finite strains. Int J Plast 46:37–53

Engler O, Crumbach M, Li S (2005) Alloy-dependent rolling texture simulation of aluminium alloys with a grain-interaction model. Acta Mater 53(8):2241–2257

Engler O, Hirsch J (2002) Texture control by thermomechanical processing of AA6xxx Al–Mg–Si sheet alloys for automotive applications—a review. Mat Sci Eng A 336(1–2):249–262

Eshelby JD (1957) The determination of the elastic field of an ellipsoidal inclusion, and related problems. Proc R Soc A Math Phys Eng Sci 241(1226):376–396

Evers LP, Parks DM, Brekelmans WAM, Geers MGD (2002) Crystal plasticity model with enhanced hardening by geometrically necessary dislocation accumulation. J Mech Phys Solids 50(11):2403–2424

Eyckens P, Mulder H, Gawad J, Vegter H, Roose D, van den Boogaard TH, Van Bael A, Van Houtte P (2015) The prediction of differential hardening behaviour of steels by multi-scale crystal plasticity modelling. Int J Plast accepted (available on-line)

Feyel F (1999) Multiscale FE2 elastoviscoplastic analysis of composite structures. Comput Mater Sci 16(1–4):344–354

Feyel F (2003) A multilevel finite element method (FE2) to describe the response of highly non-linear structures using generalized continua. Comput Methods Appl Mech Eng 192(28–30):3233–3244

Feyel F, Chaboche J-L (2000) FE2 multiscale approach for modelling the elastoviscoplastic behaviour of long fibre SiC/Ti composite materials. Comput Methods Appl Mech Eng 183(3–4):309–330

Galán J, Verleysen P, Lebensohn RA (2014) An improved algorithm for the polycrystal viscoplastic self-consistent model and its integration with implicit finite element schemes. Model Simul Mater Sci Eng 22(5):055023

Gambin W (1992) Refined analysis of elastic-plastic crystals. Int J Solids Struct 29(16):2013–2021

Gambin W, Barlat F (1997) Modeling of deformation texture development based on rate independent crystal plasticity. Int J Plast 13(1–2):75–85

Gawad J, Van Bael A, Eyckens P, Van Houtte P, Samaey G, Roose D (2010) Effect of texture evolution in cup drawing predictions by multiscale model. Steel Res Int 81(Supplement Metal Forming):1430–1433

Gawad J, Van Bael A, Eyckens P, Samaey G, Van Houtte P, Roose D (2013) Hierarchical multi-scale modeling of texture induced plastic anisotropy in sheet forming. Comp Mater Sci 66:65–83

Gawad J, Banabic D, Van Bael A, Comsa DS, Gologanu M, Eyckens P, Van Houtte P, Roose D (2015) An evolving plane stress yield criterion based on crystal plasticity virtual experiments. Int J Plast 75:141–169

Geers MGD, Kouznetsova VG, Brekelmans WAM (2010) Multi-scale computational homogenization: trends and challenges. J Comput Appl Math 234(7):2175–2182

Ghosh S, Dimiduk D (eds) (2011) Computational methods for microstructure-property relationships. Springer, US

Gottstein G (2004) Physical foundations of materials science. Springer, Berlin

Grytten F, Holmedal B, Hopperstad OS, Børvik T (2008) Evaluation of identification methods for YLD2004-18p. Int J Plast 24(12):2248–2277

Habraken AM, Duchêne L (2004) Anisotropic elasto-plastic finite element analysis using a stress-strain interpolation method based on a polycrystalline model. Int J Plast 20(8–9):1525–1560

He WJ, Zhang SH, Prakash A, Helm D (2014) A hierarchical multi-scale model for hexagonal materials taking into account texture evolution during forming simulation. Comp Mater Sci 82:464–475

Héripré E, Dexet M, Crépin J, Gélébart L, Roos A, Bornert M, Caldemaison D (2007) Coupling between experimental measurements and polycrystal finite element calculations for micromechanical study of metallic materials. Int J Plast 23(9):1512–1539

Hill R (1948) A theory of the yielding and plastic flow of anisotropic metals. Proc Roy Form London A193:281–297

Hosford WF (1979) On yield loci of anisotropic cubic metals. In: Proceedings of the 7th North American metalworking conference (NMRC), SME, Dearborn, pp 191–197
Inal K, Mishra RK, Cazacu O (2010) Forming simulation of aluminum sheets using an anisotropic yield function coupled with crystal plasticity theory. Int J Solids Struct 47(17):2223–2233
Jung K-H, Kim D-K, Im Y-T, Lee Y-S (2013) Prediction of the effects of hardening and texture heterogeneities by finite element analysis based on the Taylor model. Int J Plast 42:120–140
Kalidindi SR, Schoenfeld SE (2000) On the prediction of yield surfaces by the crystal plasticity models for fcc polycrystals. Mater Sci Eng A 293(1–2):120–129
Kalidindi SR, Duvvuru HK (2005) Spectral methods for capturing crystallographic texture evolution during large plastic strains in metals. Acta Mater 53(13):3613–3623
Kalidindi SR, Bronkhorst CA, Anand L (1992) Crystallographic texture evolution in bulk deformation processing of FCC metals. J Mech Phys Solids 40(3):537–569
Kalidindi SR, Duvvuru HK, Knezevic M (2006) Spectral calibration of crystal plasticity models. Acta Mater 54(7):1795–1804
Kalidindi SR, Houskamp JR, Lyons M, Adams BL (2004) Microstructure sensitive design of an orthotropic plate subjected to tensile load. Int J Plast 20(8–9):1561–1575
Kalidindi SR, Knezevic M, Niezgoda S, Shaffer J (2009) Representation of the orientation distribution function and computation of first-order elastic properties closures using discrete Fourier transforms. Acta Mater 57(13):3916–3923
Kanit T, Forest S, Galliet I, Mounoury V, Jeulin D (2003) Determination of the size of the representative volume element for random composites: statistical and numerical approach. Int J Solids Struct 40(13–14):3647–3679
Kim D, Barlat F, Bouvier S, Rabahallah M, Balan T, Chung K (2007) Non-quadratic anisotropic potentials based on linear transformation of plastic strain rate. Int J Plast 23(8):1380–1399
Kim JH, Lee M-G, Barlat F, Wagoner RH, Chung K (2008) An elasto-plastic constitutive model with plastic strain rate potentials for anisotropic cubic metals. Int J Plast 24(12):2298–2334
Klusemann B, Svendsen B, Vehoff H (2012) Investigation of the deformation behavior of Fe–3 % Si sheet metal with large grains via crystal plasticity and finite-element modeling. Comput Mater Sci 52(1):25–32
Klusemann B, Svendsen B, Vehoff H (2013) Modeling and simulation of deformation behavior, orientation gradient development and heterogeneous hardening in thin sheets with coarse texture. Int J Plast 50:109–126
Knap J, Barton NR, Hornung RD, Arsenlis A, Becker R, Jefferson DR (2008) Adaptive sampling in hierarchical simulation. Int J Numer Methods Eng 76(4):572–600
Knezevic M, Kalidindi SR (2007) Fast computation of first-order elastic-plastic closures for polycrystalline cubic-orthorhombic microstructures. Comput Mater Sci 39(3):643–648
Knezevic M, Landry NW (2015) Procedures for reducing large datasets of crystal orientations using generalized spherical harmonics. Mech Mater 88:73–86
Knezevic M, Kalidindi SR, Fullwood D (2008) Computationally efficient database and spectral interpolation for fully plastic Taylor-type crystal plasticity calculations of face-centered cubic polycrystals. Int J Plast 24(7):1264–1276
Knezevic M, Al-Harbi HF, Kalidindi SR (2009) Crystal plasticity simulations using discrete Fourier transforms. Acta Mater 57(6):1777–1784
Knezevic M, Beyerlein IJ, Brown DW, Sisneros TA, Tomé CN (2013a) A polycrystal plasticity model for predicting mechanical response and texture evolution during strain-path changes: application to beryllium. Int J Plast 49:185–198
Knezevic M, Lebensohn RA, Cazacu O, Revil-Baudard B, Proust G, Vogel SC, Nixon ME (2013b) Modeling bending of α-titanium with embedded polycrystal plasticity in implicit finite elements. Mater Sci Eng A 564:116–126
Knezevic M, McCabe RJ, Lebensohn RA, Tomé CN, Liu C, Lovato ML, Mihaila B (2013c) Integration of self-consistent polycrystal plasticity with dislocation density based hardening laws within an implicit finite element framework: application to low-symmetry metals. J Mech Phys Solids 61(10):2034–2046

Kouznetsova VG, Geers MGD, Brekelmans WAM (2004a) Size of a representative volume element in a second-order computational homogenization framework. Int J Multiscale Comput Eng 2(4):575–598

Kouznetsova VG, Geers MGD, Brekelmans WAM (2004b) Multi-scale second-order computational homogenization of multi-phase materials: a nested finite element solution strategy. Comput Methods Appl Mech Eng 193(48–51):5525–5550

Kouznetsova VG, Geers MGD (2008) A multi-scale model of martensitic transformation plasticity. Mech Mater 40(8):641–657

Kowalczyk K, Gambin W (2004) Model of plastic anisotropy evolution with texture-dependent yield surface. Int J Plast 20(1):19–54

Kraska M, Doig M, Tikhorimov D, Raabe D, Roters F (2009) Virtual material testing for stamping simulations based on polycrystal plasticity. Comp Mat Sci 46:383–392

Larsson F, Runesson K (2011) On two-scale adaptive FE analysis of micro-heterogeneous media with seamless scale-bridging. Comput Methods Appl Mech Eng 200(37–40):2662–2674

Lazarescu L, Comsa DS, Banabic D (2011) Analytical and experimental evaluation of the stress-strain curves of sheet metals by hydraulic bulge test. Key Eng Mater 473:352–359

Lebensohn RA (2001) N-site modeling of a 3D viscoplastic polycrystal using fast Fourier transform. Acta Mater 49(14):2723–2737

Lebensohn RA, Tomé CN (1993) A self-consistent anisotropic approach for the simulation of plastic deformation and texture development of polycrystals: application to zirconium alloys. Acta Metall Mater 41:2611–2624

Lebensohn RA, Liu Y, Ponte Castañeda P (2004) On the accuracy of the self-consistent approximation for polycrystals: comparison with full-field numerical simulations. Acta Mater 52(18):5347–5361

Lebensohn RA, Tomé CN, Ponte Castañeda P (2007) Self-consistent modelling of the mechanical behaviour of viscoplastic polycrystals incorporating intragranular field fluctuations. Philos Mag 87(28):4287–4322

Lebensohn RA, Brenner R, Castelnau O, Rollett AD (2008) Orientation image-based micromechanical modelling of subgrain texture evolution in polycrystalline copper. Acta Mater 56 (15):3914–3926

Lebensohn RA, Rollett AD, Suquet P (2011) Fast Fourier transform-based modeling for the determination of micromechanical fields in polycrystals. JOM 63(3):13–18

Lebensohn RA, Kanjarla AK, Eisenlohr P (2012) An elasto-viscoplastic formulation based on fast Fourier transforms for the prediction of micromechanical fields in polycrystalline materials. Int J Plast 32–33:59–69

Lequeu Ph, Gilormini P, Montheillet F, Bacroix B, Jonas JJ (1987) Yield surfaces for textured polycrystals-I. Crystallographic approach. Acta Metall 35(2):439–451

Li DS, Garmestani H, Schoenfeld S (2003) Evolution of crystal orientation distribution coefficients during plastic deformation. Mat Mater 49(9):867–872

Li S, Van Houtte P, Kalidindi SR (2004) A quantitative evaluation of the deformation texture predictions for aluminium alloys from crystal plasticity finite element method. Model Simul Mater Sci Eng 12(5):845–870

Lim H, Lee M-G, Kim JH, Adams BL, Wagoner RH (2011) Simulation of polycrystal deformation with grain and grain boundary effects. Int J Plast 27(9):1328–1354

Lim H, Carroll JD, Battaile CC, Buchheit TE, Boyce BL, Weinberger CR (2014) Grain-scale experimental validation of crystal plasticity finite element simulations of tantalum oligocrystals. Int J Plast 60:1–18

Liu YS, Delannay L, Van Houtte P (2002) Application of the Lamel model for simulating cold rolling texture in molybdenum sheet. Acta Mater 50(7):1849–1856

Liu B, Raabe D, Roters F, Eisenlohr P, Lebensohn RA (2010) Comparison of finite element and fast Fourier transform crystal plasticity solvers for texture prediction. Model Simul Mater Sci Eng 18(8):085005

Logé RE, Chastel YB (2006) Coupling the thermal and mechanical fields to metallurgical evolutions within a finite element description of a forming process. Comput Methods Appl Mech Eng 195(48–49):6843–6857
Mahesh S (2010) A binary-tree based model for rate-independent polycrystals. Int J Plast 26 (1):42–64
Mánik T, Holmedal B (2013) Additional relaxations in the Alamel texture model. Mat Sci Eng A 580:349–354
Mánik T, Holmedal B (2014) Review of the Taylor ambiguity and the relationship between rate-independent and rate-dependent full-constraints Taylor models grain interaction model. Int J Plast 55:152–181
Mathur KK, Dawson PR (1989) On modeling the development of crystallographic texture in bulk forming processes. Int J Plast 5(1):67–94
Mathur KK, Dawson PR (1990) texture development during wire drawing. J Eng Mater Technol 112(3):292
McDowell DL (2010) A perspective on trends in multiscale plasticity. Int J Plast 26(9):1280–1309
Mellbin Y, Hallberg H, Ristinmaa M (2014) Accelerating crystal plasticity simulations using GPU multiprocessors. Int J Numer Methods Eng 100(2):111–135
Miehe C (1996) Numerical computation of algorithmic (consistent) tangent moduli in large-strain computational inelasticity. Comput Methods Appl Mech Eng 134(3–4):223–240
Miehe C, Schröder J, Schotte J (1999) Computational homogenization analysis in finite plasticity Simulation of texture development in polycrystalline materials. Comput Methods Appl Mech Eng 171(3–4):387–418
Molinari A, Canova GR, Ahzi S (1987) A self consistent approach of the large deformation polycrystal viscoplasticity. Acta Metall 35(12):2983–2994
Molinari A, Ahzi S, Kouddane R (1997) On the self-consistent modeling of elastic-plastic behavior of polycrystals. Mech Mater 26(1):43–62
Nixon ME, Cazacu O, Lebensohn RA (2010a) Anisotropic response of high-purity α-titanium: Experimental characterization and constitutive modeling. Int J Plast 26(4):516–532
Nixon ME, Lebensohn RA, Cazacu O, Liu C (2010b) Experimental and finite-element analysis of the anisotropic response of high-purity α-titanium in bending. Acta Mater 58(17):5759–5767
Ostoja-Starzewski M (2005) Scale effects in plasticity of random media: status and challenges. Int J Plast 21(6):1119–1160
Ostoja-Starzewski M (2006) Material spatial randomness: from statistical to representative volume element. Probab Eng Mech 21(2):112–132
Peirce D, Asaro RJ, Needleman A (1982) An analysis of nonuniform and localized deformation in ductile single crystals. Acta Metall 30(6):1087–1119
Peirce D, Asaro RJ, Needleman A (1983) Material rate dependence and localized deformation in crystalline solids. Acta Metall 31(12):1951–1976
Pinna C, Lan Y, Kiu MF, Efthimiadis P, Lopez-Pedrosa M, Farrugia D (2015) Assessment of crystal plasticity finite element simulations of the hot deformation of metals from local strain and orientation measurements. Int J Plast 73:24–38
Plunkett B, Lebensohn RA, Cazacu O, Barlat F (2006) Anisotropic yield function of hexagonal materials taking into account texture development and anisotropic hardening. Acta Mater 54 (16):4159–4169
Plunkett B, Cazacu O, Barlat F (2008) Orthotropic yield criteria for description of the anisotropy in tension and compression of sheet metals. Int J Plast 24(5):847–866
Pokharel R, Lind J, Kanjarla AK, Lebensohn RA, Li SF, Kenesei P, Suter RM, Rollett AD (2014) Polycrystal plasticity: comparison between grain—scale observations of deformation and simulations. Annu Rev Condens Matter Phys 5(1):317–346
Prakash A, Lebensohn RA (2009) Simulation of micromechanical behavior of polycrystals: finite elements versus fast Fourier transforms. Model Simul Mater Sci Eng 17(6):064010
Prakash A, Nöhring WG, Lebensohn RA, Höppel HW, Bitzek E (2015) A multiscale simulation framework of the accumulative roll bonding process accounting for texture evolution. Mater Sci Eng A 631:104–119

Quey R, Dawson PR, Barbe F (2011) Large-scale 3D random polycrystals for the finite element method: generation, meshing and remeshing. Comput Methods Appl Mech Eng 200(17–20):1729–1745

Raabe D, Roters F (2004) Using texture components in crystal plasticity finite element simulations. Int J Plast 20(3):339–361

Raabe D, Zhao Z, Roters F (2004) Study on the orientational stability of cube-oriented FCC crystals under plane strain by use of a texture component crystal plasticity finite element method. Mat Mater 50(7):1085–1090

Raabe D, Sachtleber M, Zhao Z, Roters F, Zaefferer S (2001) Micromechanical and macromechanical effects in grain scale polycrystal plasticity experimentation and simulation. Acta Mater 49(17):3433–3441

Rabahallah M, Balan T, Bouvier S, Bacroix B, Barlat F, Chung K, Teodosiu C (2009) Parameter identification of advanced plastic strain rate potentials and impact on plastic anisotropy prediction. Int J Plast 25(3):491–512

Raphanel JL, Van Houtte P (1985) Simulation of the rolling textures of b.c.c. metals by means of the relaxed Taylor theory. Acta Metall 33(8):1481–1488

Reis FJP, Andrade Pires FM (2013) An adaptive sub-incremental strategy for the solution of homogenization-based multi-scale problems. Comput Methods Appl Mech Eng 257:164–182

Resk H, Delannay L, Bernacki M, Coupez T, Logé R (2009) Adaptive mesh refinement and automatic remeshing in crystal plasticity finite element simulations. Model Simul Mater Sci Eng 17(7):075012

Roters F (2005) Application of crystal plasticity FEM from single crystal to bulk polycrystal. Comput Mater Sci 32(3–4):509–517

Roters F, Eisenlohr P, Hantcherli L, Tjahjanto DD, Bieler TR, Raabe D (2010a) Overview of constitutive laws, kinematics, homogenization and multiscale methods in crystal plasticity finite-element modeling: theory, experiments, applications. Acta Mater 58(4):1152–1211

Roters F, Eisenlohr P, Bieler TR, Raabe D (2010b) Crystal plasticity finite element methods. Wiley-VCH Verlag GmbH & Co, KGaA

Roters F, Eisenlohr P, Kords C, Tjahjanto DD, Diehl M, Raabe D (2012) DAMASK: the Düsseldorf Advanced MAterial Simulation Kit for studying crystal plasticity using an FE based or a spectral numerical solver. Procedia IUTAM 3:3–10

Rouet-Leduc B, Barros K, Cieren E, Elango V, Junghans C, Lookman T, Mohd-Yusof J, Pavel RS, Rivera AY, Roehm D, McPherson AL, Germann TC (2014) Spatial adaptive sampling in multiscale simulation. Comput Phys Commun 185(7):1857–1864

Rousselier G, Leclercq S (2006) A simplified "polycrystalline" model for viscoplastic and damage finite element analyses. Int J Plast 22(4):685–712

Rousselier G, Barlat F, Yoon JW (2009) A novel approach for anisotropic hardening modeling. Part I: Theory and its application to finite element analysis of deep drawing. Int J Plast 25 (12):2383–2409

Saai A, Dumoulin S, Hopperstad OS, Lademo OG (2013) Simulation of yield surfaces for aluminium sheets with rolling and recrystallization textures. Comp Mater Sci 67:424–433

Sachs G (1928) Zur ableitung einer filebedingung. Zeitschrift des Vereines Deutscher Ingenieure 72:734–736

Savoie J, MacEwen SR (1996) A sixth order inverse potential function for incorporation of crystallographic texture into predictions of properties of aluminium sheet. Texture MicroStruct 26(C):495–512

Schoenfeld SE (1998) Dynamic behaviour of polycrystalline tantalum. Int J Plast 14(9):871–890

Segurado J, Lebensohn RA, LLorca J, Tomé CN (2012) Multiscale modeling of plasticity based on embedding the viscoplastic self-consistent formulation in implicit finite elements. Int J Plast 28 (1):124–140

Shaffer JB, Knezevic M, Kalidindi SR (2010) Building texture evolution networks for deformation processing of polycrystalline fcc metals using spectral approaches: applications to process design for targeted performance. Int J Plast 26(8):1183–1194

Shanthraj P, Eisenlohr P, Diehl M, Roters F (2015) Numerically robust spectral methods for crystal plasticity simulations of heterogeneous materials. Int J Plast 66:31–45

Smit RJM, Brekelmans WAM, Meijer HEH (1998) Prediction of the mechanical behavior of nonlinear heterogeneous systems by multi-level finite element modeling. Comput Methods Appl Mech Eng 155(1–2):181–192

Soare S, Barlat F (2010) Convex polynomial yield functions. J Mech Phys Solids 58(11):1804–1818

Soare S, Whan Yoon J, Cazacu O (2008) On the use of homogeneous polynomials to develop anisotropic yield functions with applications to sheet forming. Int J Plast 24(6):915–944

St-Pierre L, Héripré E, Dexet M, Crépin J, Bertolino G, Bilger N (2008) 3D simulations of microstructure and comparison with experimental microstructure coming from O.I.M analysis. Int J Plast 24(9):1516–1532

Steglich D, Jeong Y, Andar MO, Kuwabara T (2012) Biaxial deformation behaviour of AZ31 magnesium alloy: crystal-plasticity-based prediction and experimental validation. Int J Solids Struct 49(25):3551–3561

Taylor GI (1938) Plastic strain in metals. J Inst Metals 62:307–324

Temizer I, Wriggers P (2008) On the computation of the macroscopic tangent for multiscale volumetric homogenization problems. Comput Methods Appl Mech Eng 198(3–4):495–510

Temizer I, Wriggers P (2011) An adaptive multiscale resolution strategy for the finite deformation analysis of microheterogeneous structures. Comput Methods Appl Mech Eng 200(37–40):2639–2661

Tjahjanto DD, Eisenlohr P, Roters F (2010) A novel grain cluster-based homogenization scheme. Modell Simul Mater Sci Eng 18(1):015006

Tjahjanto DD, Eisenlohr P, Roters F (2015) Multiscale deep drawing analysis of dual-phase steels using grain cluster-based RGC scheme. Model Simul Mater Sci Eng 23(4):045005

Tomé CN (2001) Mechanical response of zirconium—I. Derivation of a polycrystal constitutive law and finite element analysis. Acta Mater 49(15):3085–3096

Tóth L-S, Van Houtte P (1992) Discretization techniques for orientation distribution functions. Texture MicroStruct 19:229–244

Tsotsova R, Böhlke T (2009) Representation of effective flow potentials for polycrystals based on texture data. Int J Mater Form 2(S1):451–454

Turner TJ, Shade PA, Schuren JC, Groeber MA (2013) The influence of microstructure on surface strain distributions in a nickel micro-tension specimen. Model Simul Mater Sci Eng 21 (1):015002

Van Bael A, Eyckens P, Gawad J, Samaey G, Roose D, Van Houtte P (2010) Evolution of crystallographic texture and mechanical anisotropy during cup drawing. Steel Res Int 81 (Supplement Metal Forming):1392–1395

Van Houtte P (1982) On the equivalence of the relaxed Taylor theory and the Bishop-Hill theory for partially constrained plastic deformation of crystals. Mater Sci Eng 55(1):69–77

Van Houtte P (1987) Calculation of the yield locus of textured polycrystals using the Taylor and the relaxed Taylor theory. Textures MicroStruct 7(C):29–72

Van Houtte P (1988) A comprehensive mathematical formulation of an extended Taylor–Bishop–Hill model featuring relaxed constraints, the Renouard–Wintenberger theory and a strain rate sensitivity model. Textures MicroStruct 8(C):313–350

Van Houtte P (1995) The MTM-FHM software system Version 2

Van Houtte P (2001) Fast calculation of average Taylor factors and Mandel spins for all possible strain modes. Int J Plast 17(6):807–818

Van Houtte P, Van Bael A (2004) Convex plastic potentials of fourth and sixth rank for anisotropic materials. Int J Plast 20(8–9):1505–1524

Van Houtte P, Delannay L, Samajdar I (1999) Quantitative prediction of cold rolling textures in low-carbon steel by means of the Lamel model. Texture MicroStruct 31(3):109–149

Van Houtte P, Delannay L, Kalidindi SR (2002) Comparison of two grain interaction models for polycrystal plasticity and deformation texture prediction. Int J Plast 18(3):359–377

Van Houtte P, Li S, Seefeldt M, Delannay L (2005) Deformation texture prediction: from the Taylor model to the advanced Lamel model. Int J Plast 21(3):589–624
Van Houtte P, Kumar Yerra S, Van Bael A (2009) The Facet method: a hierarchical multilevel modelling scheme for anisotropic convex plastic potentials. Int J Plast 25(2):332–360
Van Houtte P, Gawad J, Eyckens P, Van Bael A, Samaey G, Roose D (2011) A full-field strategy to take texture induced anisotropy into account during FE simulations of metal forming processes. JOM 63:37–43
Vegter H, van den Boogaard TH (2006) A plane stress yield function for anisotropic sheet material by interpolation of biaxial stress states. Int J Plast 22(3):557–580
Vegter H, ten Horn CHLJ, An Y, Atzema EH, Pijlman HH, van den Boogaard TH, Huétink H (2003) Characterisation and modelling of the plastic material behaviour and its application in sheet metal forming simulation. In: Oñate E, Owen DRJ (eds) Proceedings of COMPLAS VII, CIMNE, Barcelona pages (on CD-ROM)
Walde T, Riedel H (2007a) Simulation of earing during deep drawing of magnesium alloy AZ31. Acta Mater 55(3):867–874
Walde T, Riedel H (2007b) Modeling texture evolution during hot rolling of magnesium alloy AZ31. Mater Sci Eng A 443(1–2):277–284
Wang H, Wu Y, Wu PD, Neale KW (2010) Numerical analysis of large strain simple shear and fixed-end torsion of HCP polycrystals. Comput Mater Contin 19(3):255–284
Werwer M, Cornec A (2000) Numerical simulation of plastic deformation and fracture in polysynthetically twinned (PST) crystals of TiAl. Comput Mater Sci 19(1–4):97–107
Yoon JW, Barlat F, Dick RE, Karabin ME (2006) Prediction of six or eight ears in a drawn cup based on a new anisotropic yield function. Int J Plast 22(1):174–193
Yoon J-H, Cazacu O, Yoon JW, Dick RE (2010) Earing predictions for strongly textured aluminum sheets. Int J Mech Sci 52(12):1563–1578
Yoon J-W, Lou Y, Yoon J-H, Glazoff MV (2014) Asymmetric yield function based on the stress invariants for pressure sensitive metals. Int J Plast 56:184–202
Yoon J-W, Barlat F, Dick RE, Chung K, Kang TJ (2004) Plane stress yield function for aluminum alloy sheets–part II: FE formulation and its implementation. Int J Plast 20(3):495–522
Yoshida F, Hamasaki H, Uemori T (2013) A user-friendly 3D yield function to describe anisotropy of steel sheets. Int J Plast 45:119–139
Zamiri A, Pourboghrat F, Barlat F (2007) An effective computational algorithm for rate-independent crystal plasticity based on a single crystal yield surface with an application to tube hydroforming. Int J Plast 23(7):1126–1147
Zamiri AR, Pourboghrat F (2010) A novel yield function for single crystals based on combined constraints optimization. Int J Plast 26(5):731–746
Zecevic M, McCabe RJ, Knezevic M (2015a) Spectral database solutions to elasto-viscoplasticity within finite elements: Application to a cobalt-based FCC superalloy. Int J Plast 70:151–165
Zecevic M, McCabe RJ, Knezevic M (2015b) A new implementation of the spectral crystal plasticity framework in implicit finite elements. Mech Mater 84:114–126
Zhang K, Holmedal B, Hopperstad OS, Dumoulin S (2014) Modelling the plastic anisotropy of aluminum alloy 3103 sheets by polycrystal plasticity. Model Simul Mater Sci Eng 22 (7):075015
Zhang C, Li H, Eisenlohr P, Liu W, Boehlert CJ, Crimp MA, Bieler TR (2015a) Effect of realistic 3D microstructure in crystal plasticity finite element analysis of polycrystalline Ti-5Al-2.5Sn. Int J Plast 69:21–35
Zhang K, Holmedal B, Hopperstad OS, Dumoulin S, Gawad J, Van Bael A, Van Houtte P (2015b) Multi-level modelling of mechanical anisotropy of commercial pure aluminium plate: crystal plasticity models, advanced yield functions and parameter identification. Int J Plast 66:3–30
Zhao Z, Mao W, Roters F, Raabe D (2004) A texture optimization study for minimum earing in aluminium by use of a texture component crystal plasticity finite element method. Acta Mater 52(4):1003–1012